AIAA SciTech Forum
7-11 January 2019, San Diego, California
AIAA Scitech 2019 Forum

10.2514/6.2019-0079

FUN3D Juncture Flow Computations Compared with Experimental Data

C. L. Rumsey*, J.-R. Carlson†, and N. N. Ahmad‡
NASA Langley Research Center, Hampton, VA 23681

The first phase of the NASA Juncture Flow experiment, designed to experimentally investigate flowfield details in the wing-body junction region of an aircraft configuration, has been completed. The current configuration was designed to have separated flow in the corner at the wing trailing edge; the separation size varies with angle of attack. Two different angles of attack are considered. This type of junction separation has traditionally been difficult for CFD to consistently and accurately predict. This paper is one of two whose purpose is to document initial CFD efforts computing this flow, and to compare with the newly acquired experimental data. We investigate CFD's ability to predict the flowfield details leading up to separation, including progression of separation size with angle of attack. As part of this effort, a grid sensitivity study is conducted and CFD uncertainties due to discretization error are estimated. Three different Reynolds-averaged Navier-Stokes turbulence models are compared, including a linear eddy viscosity one-equation model, a nonlinear version of the same model, and a full second-moment seven-equation model.

I. Introduction

The first phase of wind tunnel testing on the NASA Juncture Flow (JF) configuration in the NASA Langley 14- by 22-Foot Subsonic Tunnel (14x22) has been completed. The main focus area for this full-span aircraft-shaped model is the junction region between the wing upper surface and body, where separated flow can occur and where CFD has historically been inaccurate and inconsistent. The purpose of this particular series of wind tunnel tests is to provide flowfield data (velocity and Reynolds stresses) in and near the wing-body junction region, along with boundary condition and geometry information, so that CFD validation can be confidently performed. Ultimately, we hope to learn how well existing turbulence models predict the flowfield features in the corner region, and gain enough insight to be able to improve the models as needed.

A significant amount of preparatory work has preceded the NASA Juncture Flow experiment [1–8]. This work included both risk-reduction experiments as well as preliminary CFD analysis, with a goal of optimizing the value of the data obtained in the final tests. The JF team initially had a goal of finding a single configuration that could achieve fully-attached flow, incipient separation, and separated corner flow by varying either Mach number or angle of attack, but this was not achieved. In the end, two different interchangeable wing configurations were built: (1) a wing based on the DLR-F6 [9] that produces separated corner flow at all angles-of-attack tested during this campaign, and (2) a wing based on the NACA 0015 shape (near its root) that produces primarily attached flow and incipient separation. In the wind tunnel campaigns performed in late 2017 through early 2018, only the former wing was tested.

The main focus of the experiment was its use of a Laser Doppler Velocimetry (LDV) system carried on board the model to measure the junction flowfield. This system was installed inside the fuselage, and its lasers were emitted through side windows on the port side. This setup allowed the collection of flowfield data to within a very small distance of the junction corner. Also, because the system was contained onboard, the influence of model motion on the data collection was minimized. The main downside to LDV is that it is a slow process, collecting data one point at a time. In this test, many lines of points were collected, giving "profile" data at various locations. Some preliminary tests using Particle Image Velocimetry (PIV) were also conducted. The advantage of PIV is that it can collect an entire plane of data simultaneously.

This paper provides comparisons of FUN3D [10, 11] CFD results with experimental data. Unfortunately, the experimental data from the test have not all been processed as of the time of this writing (in particular, pressures and

*Research Scientist, Computational AeroSciences Branch, Mail Stop 128, Fellow AIAA.
†Research Scientist, Computational AeroSciences Branch, Mail Stop 128, Associate Fellow AIAA.
‡Research Scientist, Computational AeroSciences Branch, Mail Stop 128, Senior Member AIAA.

some of the boundary condition information have not yet been fully vetted). Also, all of the intended CFD runs have not yet been completed. Therefore, these comparisons should be considered preliminary. This paper is appearing at the AIAA SciTech 2018 conference alongside other related JF papers, including one representing OVERFLOW [12] CFD comparisons, one on preliminary PIV data, and one on the JF experiment itself (including the LDV data).

II. Grids

A general view of the NASA Juncture Flow configuration is shown in Fig. 1. Note that this figure shows the wing with a leading-edge horn, or fillet. The purpose of this horn is to mitigate the strength and influence of the so-called "horseshoe" vortex that forms in front of the wing leading edge along the fuselage. Experimental data were collected both with and without the horn in place. However, the CFD results in this paper only consider the case *with* the horn. In the tunnel, the model was mounted on a sting aligned with the fuselage axis. The sting was attached to a mast that emerged from the wind tunnel floor. For all the results in this paper, both the sting and mast were ignored. The computed configuration is as shown in this figure.

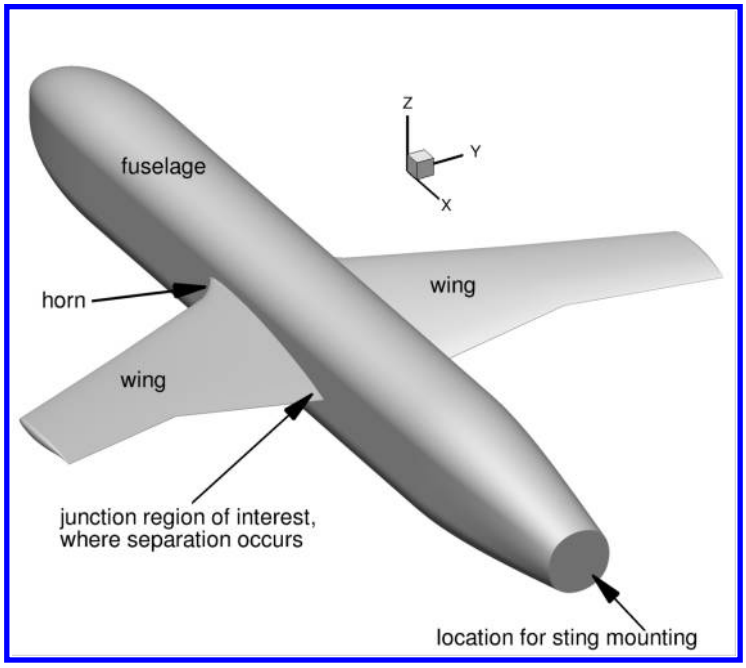

Figure 1. The NASA Juncture Flow configuration.

The shape used in the CFD for this study was from the original *as-designed* computer aided design (CAD) model. Laser scans and photogrammetry measurements were made of the model for the purpose of helping to determine the *as-built* shape (including aeroelastic deflection), but that information has not been fully processed yet, so is not included in the current study. Preliminary analysis suggests that the influence of wing aeroelasticity is relatively minor, particularly in the junction region of interest. It is also important to note that the experimental model was tripped near the front of the fuselage and on the upper and lower surfaces of both wings. In the current CFD study, all models were run "fully turbulent." The model wing span was nominally 3397.250 mm, fuselage length was 4839.233 mm, and crank chord (the chord at the y-station with trailing edge break) was 557.17 mm. The fuselage nose was taken to be at $x = 0$, the x axis was aligned with the fuselage centerline, the y axis ran starboard, and the z axis was up. The fuselage side wall was planar over much of the body (to make it easier to install windows for the laser-based measurement systems), at $y = -236.098$ mm. The F6 wing leading edge horn was located near $x = 1925$ mm at the fuselage, while the F6 wing root trailing edge was located at $x = 2961.929$ mm.

To date, only free air grids (extending to the far field) with symmetry plane along the x-z axis have been employed for this study. Some initial runs on grids including wind tunnel walls have been made using a proportional-integral-derivative (PID) controller [13], but more progress is required before results can be shown. The free-air grids were created using VGRID [14], version 4.10. The far field extent was $-55,880 \leq x \leq 55,880$ mm, $-55,880 \leq z \leq 55,880$ mm, and $-55,880 \leq y \leq 0$ mm. Four unstructured grid levels were created, with an attempt to maintain

characteristics consistent for grids in the same family. Some details are provided in Table 1. However, note that it proved to be too difficult to create an extra-fine (XF) grid with the desired parameters (VGRID could not handle the high element count), so the XF grid is not as fine as it should be. For example, the number of unknowns (N) increases by a factor of about 3.3 between C $\rightarrow$ M and between M $\rightarrow$ F, but only increases by a factor of about 2.1 between F $\rightarrow$ XF. Therefore, it is highly unlikely that the XF grid is in a similar "family" as the other three grids. The original grids were all tetrahedral, but the tetrahedra were merged into prisms in the boundary layer regions (this process results in some pyramids near the edge of the boundary layer). To give a feel for the spacing near the wing trailing edge at the wing-body juncture, there were approximately 5 grid points across the blunt trailing edge face on the C grid, 8 on the M grid, 11 on the F grid, and 15 on the XF grid.

Table 1. Summary of free-air half-span grids

Grid	Number of unknowns (N)	Tets / Prisms / Pyramids (millions)	Minimum wall spacing (mm)	Stretching rate near walls
Coarse (C)	10,698,282	50 / 4 / 0.02	0.000675	1.25
Medium (M)	35,714,223	165 / 15 / 0.05	0.00045	1.16
Fine (F)	120,425,570	553 / 52 / 0.11	0.0003	1.10
X-Fine (XF)	258,369,110	1192 / 110 / 0.14	0.0002	1.07

Figure 2 shows the surface grids for each of the grid levels on the inner area of the wing and part of the fuselage. The spacing was refined to some degree near the wing leading edge, trailing edge, and root. Views of the grids at a constant x station near the wing trailing edge are shown in Fig. 3. Most of the computations to date have been performed only on the Coarse and Medium grid levels, but we will show the influence of the Fine and X-Fine levels for one of the turbulence models. Ultimately, as a result of this study, we hope to determine the influence of the grid density on the flowfield characteristics of interest, so that we can fully account for the effects of discretization error and more confidently draw conclusions regarding turbulence model efficacy in the future. Other ongoing work is exploring the influence of targeted grid refinement (in the juncture region) as well as automated adaptive mesh refinement. Neither of these ongoing efforts are described in this paper.

III. Numerical Method

The NASA FUN3D [10, 11] solver is an unstructured three-dimensional, implicit, Navier-Stokes code that is nominally second-order spatially accurate. Roe's flux difference splitting [15] is used for the calculation of the inviscid terms for all the results in this paper (other flux construction methods are also available). The use of flux limiters are grid and flow dependent (none were used here). Other details regarding the code can be found in the extensive bibliography that is accessible at the FUN3D website [16].

For the free-air computations, a farfield Riemann invariant boundary condition was imposed on the outer boundary, no-slip solid wall boundary conditions were applied on the model, and symmetry conditions were used on the x-z symmetry plane.

A. Turbulence Models

The turbulence models tested so far for this study were SA-RC [17, 18], SA-RC-QCR2013 [19], and SSG/LRR-RSM-w2012-SD [20, 21]. (To save space, the latter model is referred to simply as RSM in the remainder of the paper.) It should be noted that in FUN3D, the implementation of QCR2013 encountered significant numerical difficulties on all grids tested. In this model, the Reynolds stresses (τ_{ij}) are modified via:

$$\tau_{ij,QCR} = \tau_{ij} - C_{cr1}\left[O_{ik}\tau_{jk} + O_{jk}\tau_{ik}\right] - C_{cr2}\mu_t\sqrt{2S^*_{mn}S^*_{mn}}\delta_{ij} \tag{1}$$

where

$$O_{ij} = 2W_{ij}/\sqrt{\frac{\partial u_m}{\partial x_n}\frac{\partial u_m}{\partial x_n}} \tag{2}$$

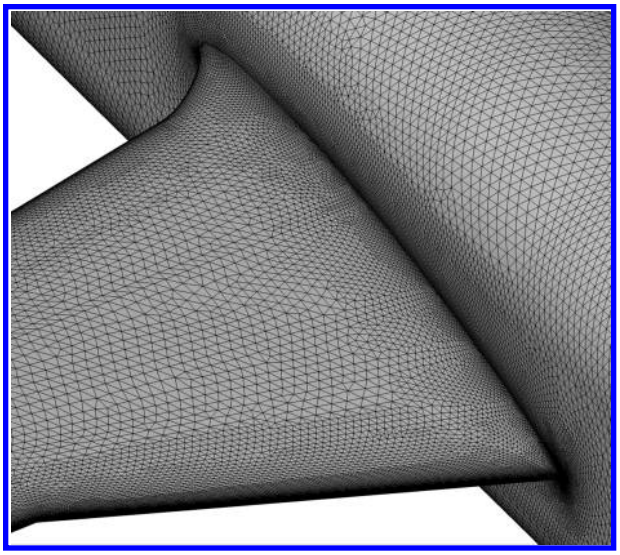

(a) Coarse (C)

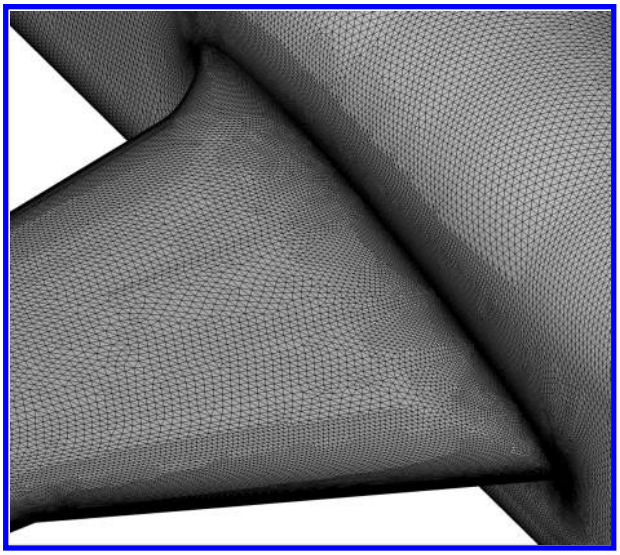

(b) Medium (M)

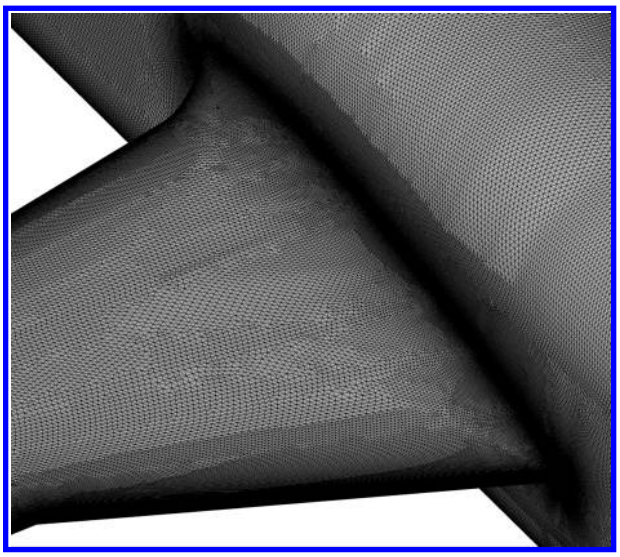

(c) Fine (F)

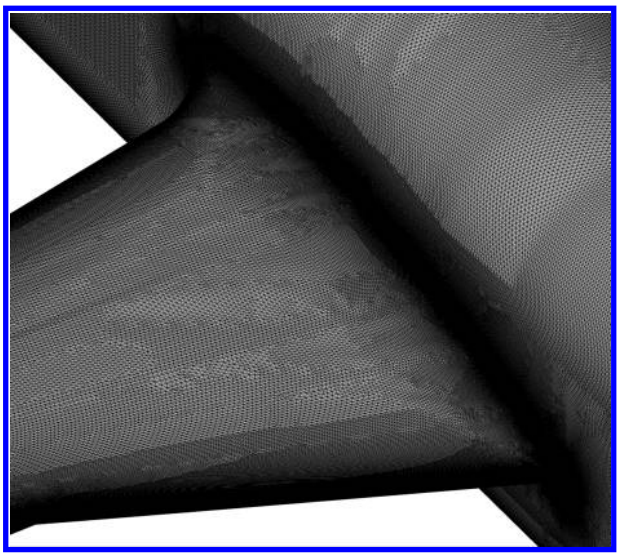

(d) Extra Fine (XF)

Figure 2. Views of surface grids.

$$W_{ij} = (\partial u_i/\partial x_j - \partial u_j/\partial x_i)/2 \tag{3}$$

$$\sqrt{\frac{\partial u_m}{\partial x_n}\frac{\partial u_m}{\partial x_n}} = \sqrt{u_x^2 + u_y^2 + u_z^2 + v_x^2 + v_y^2 + v_z^2 + w_x^2 + w_y^2 + w_z^2} \tag{4}$$

$$S_{ij}^* = S_{ij} - \frac{1}{3}\frac{\partial u_k}{\partial x_k}\delta_{ij} \tag{5}$$

$$S_{ij} = (\partial u_i/\partial x_j + \partial u_j/\partial x_i)/2 \tag{6}$$

The constants are $C_{cr1} = 0.3$ and $C_{cr2} = 2.5$.

We found that numerical problems can occur due to the last term in Eq. (1). This term (whose intent is to mimic the $-2\rho k\delta_{ij}/3$ term in the Boussinesq relation) is not present in the original QCR2000 [22] version. During the iterative solution process, in wake regions where μ_t is not small, the computed shear stress from QCR2013 could deviate

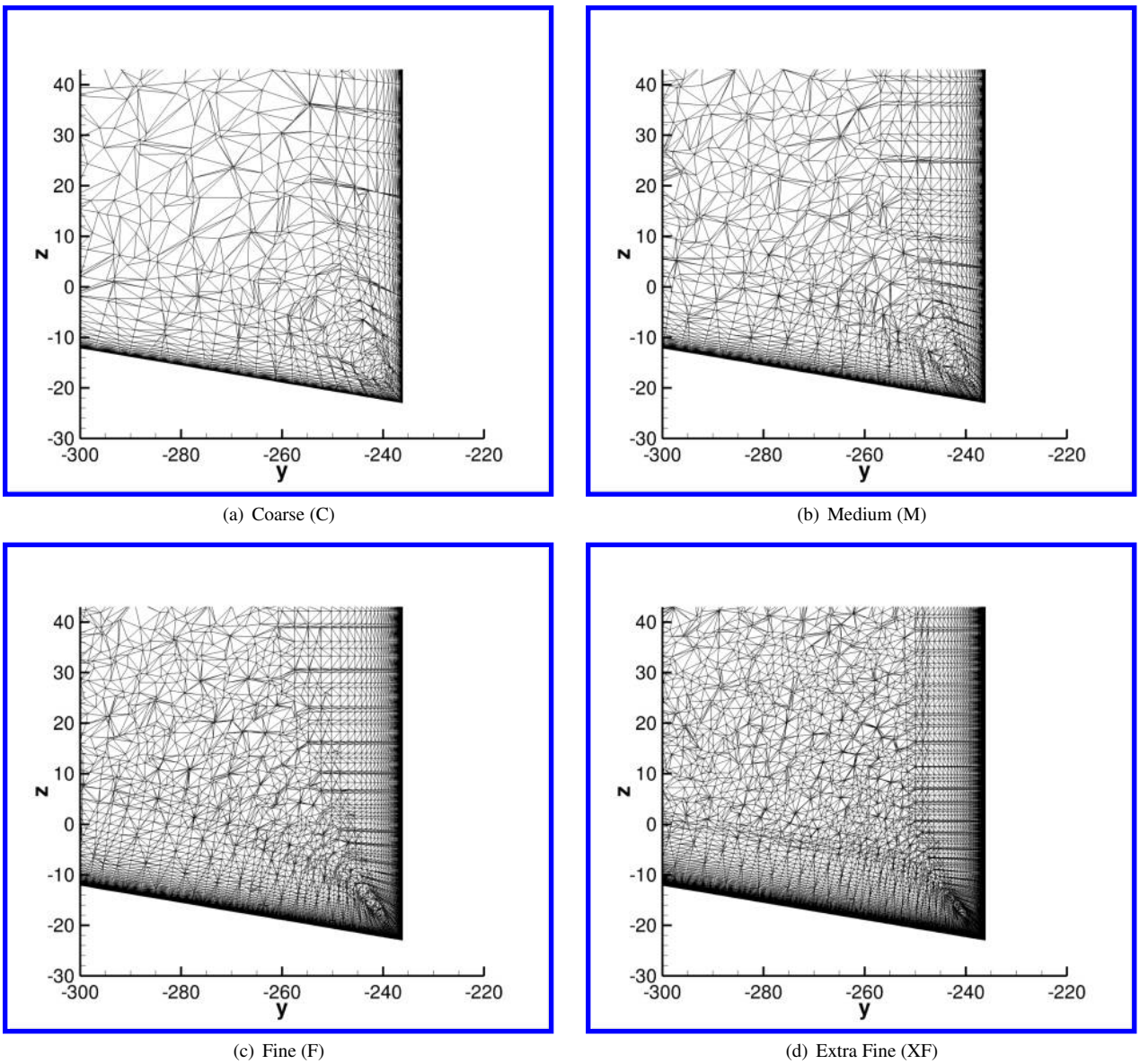

(a) Coarse (C)

(b) Medium (M)

(c) Fine (F)

(d) Extra Fine (XF)

Figure 3. Views of grid cross sections (units in mm) at $x = 2899.6$ mm (62.33 mm upstream of the wing trailing edge).

enough to yield local τ_{ij} levels that cause the solution to diverge. Our fix at this time is to impose a limiter so that the problematic term becomes:

$$-C_{cr2}\mu_t \left[\min\left(\sqrt{2S^*_{mn}S^*_{mn}}, A\sqrt{2W_{mn}W_{mn}}\right)\right]\delta_{ij} \tag{7}$$

where A was chosen to be between 1.2 and 2 (finer grids required smaller values).

It should also be noted that the implementation of RSM in FUN3D is not as numerically robust as other models. With seven transport equations, this model can exhibit stiffness and difficulties converging. For the current free-air cases, we were unable to attain converged RSM results on the F or XF grids. However, its residuals converged well (between 5 and 6 orders of magnitude) on the C and M grids. For the SA-RC and SA-RC-QCR2013 models, mean flow and turbulence residuals typically converged at least 6 orders of magnitude.

IV. CFD Uncertainty Procedure

The basic uncertainty estimation procedure from the Fluids Engineering Division of the ASME [23] is employed, along with some minor variations. The goal of this procedure is to establish CFD uncertainty bounds due to the numerical discretization error. Three representative grid sizes, h_i, are obtained from the three finest grids. This is done using:

$$h_i = \left(\frac{1}{N_i}\right)^A \tag{8}$$

where N_i is the number of unknowns (grid size) for the ith grid and $A = 1/2$ for 2-D and $1/3$ for 3-D. The grids should be in the same "family." For example, in a structured-grid family, each successively coarser grid is formed by taking every other grid point in each coordinate direction from the next finer grid. The grid ratios are defined as:

$$r_{21} \equiv h_2/h_1 \qquad r_{32} \equiv h_3/h_2 \tag{9}$$

where h_1 represents the finest of the three grids, and h_3 the coarsest. Then, with ϕ_1, ϕ_2, and ϕ_3 representing the corresponding three solutions on each grid, the solution differences are defined as:

$$\varepsilon_{21} \equiv \phi_2 - \phi_1 \qquad \varepsilon_{32} \equiv \phi_3 - \phi_2 \tag{10}$$

The apparent order p is found using fixed point iteration from the following:

$$p = \frac{1}{ln(r_{21})}(ln|\varepsilon_{32}/\varepsilon_{21}| + q(p)) \tag{11}$$

$$q(p) = ln\left(\frac{r_{21}^p - s}{r_{32}^p - s}\right) \tag{12}$$

$$s = 1 \times sign(\varepsilon_{32}/\varepsilon_{21}) \tag{13}$$

Note that if $\varepsilon_{32}/\varepsilon_{21} \leq 0$ then the convergence is "oscillatory" (non-monotonic). Also note that the above expression for p above is different than the expression in Ref. [23], in that the absolute value is *not* taken of the quantity $(ln|\varepsilon_{32}/\varepsilon_{21}| + q(p))$. This is because we want to be able to recognize when the apparent computed order is nonpositive (divergent).

The approximate relative fine-grid error is:

$$e_a^{21} = \left|\frac{\phi_1 - \phi_2}{\phi_1}\right| \tag{14}$$

The extrapolated relative fine-grid error is:

$$e_{ext}^{21} = \left|\frac{\phi_{ext}^{21} - \phi_1}{\phi_{ext}^{21}}\right| \tag{15}$$

where ϕ_{ext}^{21} is the extrapolated value of the solution using:

$$\phi_{ext}^{21} = (r_{21}^p \phi_1 - \phi_2)/(r_{21}^p - 1) \tag{16}$$

The basic fine-grid convergence index, GCI_{fine}^{21}, is computed from:

$$GCI_{fine}^{21} = \frac{1.25 e_a^{21}}{r_{21}^p - 1} \tag{17}$$

where the 1.25 in the expression is the recommended "safety factor." The GCI_{fine}^{21} is expressed in $\%$ by multiplying it by 100. The solution itself can be expressed as the fine grid value plus or minus its uncertainty based on GCI_{fine}^{21}:

$$\phi \approx \phi_1 \pm (GCI_{fine}^{21})|\phi_1| \tag{18}$$

Further refinements to GCI_{fine}^{21} have been made based on ideas from Eça and Hoekstra [24]. When the computed apparent order p is positive, but below some cutoff value C_{low} (taken here as $C_{low} = 0.95$), the GCI_{fine}^{21} is limited

based on a factor of the maximum difference (in absolute value) between any of the solutions, $\Delta_M = max(|\phi_2 - \phi_1|, |\phi_3 - \phi_2|, |\phi_3 - \phi_1|)$:

$$GCI^{21}_{fine} = min(\frac{1.25e^{21}_a}{r^p_{21} - 1}, 1.25\Delta_M/|\phi_1|). \tag{19}$$

When the computed apparent order p is above some cutoff value C_{hi} (taken here as $C_{hi} = 3.05$), then an apparent order of $p \approx C_{hi}$ is imposed, and again GCI^{21}_{fine} is limited based on a factor of Δ_M:

$$GCI^{21}_{fine} = max(\frac{1.25e^{21}_a}{r^3_{21} - 1}, 1.25\Delta_M/|\phi_1|). \tag{20}$$

For cases with oscillatory convergence ($\varepsilon_{32}/\varepsilon_{21} \leq 0$) or for cases with nonpositive apparent order ($p \leq 0$), then determination of GCI^{21}_{fine} is more difficult. Ref. [24] suggests use of the following:

$$GCI^{21}_{fine} = 3\Delta_M/|\phi_1| \tag{21}$$

for non-monotonic convergence. Here, we use Eq. (21) for both non-monotonic convergence and nonpositive apparent order. This is purposefully a conservative estimate because the goal is to bound the "infinite grid" solution with 95% confidence.

V. Results

A. Flow Conditions

In the 14x22 wind tunnel, the Reynolds number (based on the crank chord length) was held fixed at 2.4 million ($\pm 0.3\%$) throughout the testing. However, the atmospheric conditions varied, so that the Mach number ranged from about 0.175 to 0.205, temperature ranged from about 275 to 308 K, and dynamic pressure ranged from about 2107 to 2921 Pa. In this study, we used the median values from the test of $M = 0.189$ and $T = 288.84$ K. The median dynamic pressure was approximately 2476 Pa.

Two angles of incidence were selected in the experiment for detailed data collection: nominally 5 degrees and -2.5 degrees. These choices yielded two different separation sizes (larger and smaller, respectively). The actual ranges throughout the testing were approximately $4.97 < \alpha < 5.04$ degrees and $-2.54 < \alpha < -2.48$ degrees. For this CFD study, we employed the nominal uncorrected angles of $\alpha = 5$ and -2.5 degrees for the free-air computations. Because of wind tunnel wall influence, the angles of attack used for free-air computations should be corrected. However, we do not have an accurate estimate of the corrections required because no balance data were collected in this experiment. Also, ultimately, we believe that proper validation computations for this configuration should always include the wind tunnel walls in order to minimize differences between the experimental and computational setups. Therefore, the free-air computations in this study should be viewed with caution. Their primary purpose is to assess grid influence and to begin to qualitatively evaluate various turbulence models against experiment. This initial CFD assessment should also help inform additional measurement needs in future testing on this model. Several parametric variations were conducted on the free-air grids, including a grid density study.

B. General Overview of Results

In past workshops (e.g., Vassberg et al. [9]), Reynolds-averaged Navier-Stokes (RANS) codes that used turbulence models with linear (Boussinesq) closures have been very inconsistent for predicting side-of-body separation sizes at wing-body junctures. More recently, progress has been made uncovering the need for nonlinear constitutive relations in junction areas, leading to better modeling of the normal Reynolds stresses [25, 26]. Here, we look at the behavior of three different turbulence models. One of them, SA-RC, is a linear (Boussinesq) model. The other two, SA-RC-QCR2013 and RSM, are nonlinear models. SA-RC-QCR2013 is the same as SA-RC except that it includes the QCR2013 quadratic constitutive relation. It is a far simpler model than RSM, solving only one transport equation. The RSM is a full second moment Reynolds stress model that requires the solution of seven transport equations.

Figure 4 shows approximate separation sizes (measured along the wing surface) from the various models, compared to experiment. For the two conditions of $\alpha = 5^\circ$ and -2.5°, the SA-RC model predicted too large a separation. On the other hand, both the SA-RC-QCR2013 and RSM predicted separation sizes relatively consistent with the experiment. For the SA-RC-QCR2013 model, the predicted size decreased significantly with increasing grid size, while the RSM predictions were only mildly sensitive to grid. However, as mentioned earlier, we were unable to converge

the RSM on the F or XF grids, so it is not clear whether the RSM solution trend would still remain relatively flat on those grid levels. Note that the XF results in the figure are plotted as a separate symbol, because this grid is not in the same family as the C, M, and F grids. Its results would therefore not be expected to necessarily lie along the same trend line. Nonetheless, the XF grid results were in closer agreement with experiment than results on the other grids.

C. Verification: Comparisons with OVERFLOW Results Using SA-RC-QCR2013

Previously, FUN3D and OVERFLOW implementations of a variety of turbulence models have been verified on the NASA Turbulence Modeling Resource (TMR) website [27]. For this case, further verification was done for the SA-RC-QCR2013 model. Examples are shown in Fig. 5, where predicted velocities and Reynolds stresses along the y direction are shown at the location $x = 1168.4$ and $z = 0$ mm, which is on the side of the fuselage well upstream of the wing. Here, the F grid results from FUN3D are compared with results from OVERFLOW on its fine grid. The results were nearly identical for all flowfield quantities. Although not shown, agreement between the codes at many other locations was also excellent. However, noticeable differences occurred within and near separation, indicative of the fact that grid resolution and/or lack of sufficient iterative convergence were still playing a role in that region (grid sensitivity of the separation size was also evident in Fig. 4, and is discussed further below).

D. Grid Study Using SA-RC-QCR2013

Figure 4 showed overall results for prediction of separation size as a function of grid density. Here, we provide detailed flowfield results using the uncertainty estimation procedure described in Section IV. Using the three grids F, M, and C, uncertainty bounds were established; the plots show the F results along with these bounds. These CFD results are compared with experiment, which also includes uncertainty estimates. We focus here on two aspects: (1) locations of poor agreement, where the CFD uncertainty range does not intersect the experimental uncertainty range; and (2) locations where CFD uncertainty bounds are unusually large, indicating the need for additional grid resolution.

Figure 6 shows comparisons well upstream, on the side of the forward part of the fuselage. Data were taken here in an effort to establish an upstream boundary condition on the model. Results are shown for both $\alpha = 5^\circ$ (left column) and $\alpha = -2.5^\circ$ (right column). Figures 6(a) and (b) give velocity components, which generally were in excellent agreement, except that the CFD predicted the boundary layer thickness to be slightly larger. This overprediction may be due to the fact that CFD was run fully turbulent, whereas the model was tripped in the experiment near $x = 336$ mm on the fuselage nose. The turbulence quantities are split into two plots for each angle of attack; part 1 shows nondimensional $u'u'$, $v'v'$, and $u'w'$, while part 2 shows $w'w'$, $u'v'$, and $v'w'$. (The choice of which variables to put in each plot was made solely for the sake of avoiding too much overlap between the curves.) Again, CFD's prediction of too thick a boundary layer is evident. Also, while the CFD turbulent shear stresses ($u'v'$, $u'w'$, and $v'w'$) agreed fairly well with experiment, the normal Reynolds stresses ($u'u'$, $v'v'$, and $w'w'$) were not as well predicted. CFD tended to underpredict $u'u'$ (especially near the wall), and overpredict $v'v'$ and $w'w'$. However, note that the SA-RC-QCR2013 at least predicted a difference in the normal stresses, with (generally) $u'u' > w'w' > v'v'$; linear models (e.g., without QCR or other nonlinear treatment) predict to little normal stress differences. At this location on the nose, the CFD uncertainties were relatively small and well behaved, indicating good grid convergence properties. Although not shown, results here showed very little variation between the C, M, and F grids.

Comparisons off the fuselage in front of the wing are shown in Fig. 7 for both angles of attack. The computed velocity profiles again yielded good agreement with experiment, although the w component at $\alpha = 5^\circ$ showed a slight difference because the free-air computations did not employ a corrected angle of attack. The turbulent shear stresses $u'v'$ and $v'w'$ showed fairly good agreement, but the $u'w'$ was slightly off at $\alpha = 5^\circ$. The turbulent normal stresses showed similar disagreement compared to experiment as was seen earlier. At this station in front of the wing, the CFD uncertainty in the turbulence was rather significant over the outer part of the boundary layer. The reason for this can be seen in Fig. 8, for $\alpha = 5^\circ$ only. Looking at the turbulence predicted at this location, the solution in the outer region showed significant variation between the three grids. Typically, what you want to see are the differences *decreasing* with successive refinement. Here, the differences between C and M were about the same as between M and F in the outer region. Thus, the large CFD uncertainties seen in Fig. 7 reflect the fact that the current grids probably require additional refinement in this area in order to achieve reasonable grid convergence properties.

An overall view of the CFD results (using SA-RC-QCR2013 on the F grid) on the wing near the trailing edge junction is shown in Fig. 9 for $\alpha = 5^\circ$. Although not shown, results for $\alpha = -2.5^\circ$ were qualitatively similar, with smaller separation size. Both nondimensional u and w velocities are shown, followed by the six Reynolds stresses. In this $\alpha = 5^\circ$ case, the CFD separation initiated just upstream of the $x = 2822.6$ mm station, which is too early compared to experiment (measured to be near $x = 2850$ mm). As was shown earlier in Fig. 4, the predicted CFD

separation size using SA-RC-QCR2013 was very sensitive to the grid employed (separation decreased with increasing grid density). This sensitivity will be explored in greater detail below.

Figure 10 show comparisons on the wing, upstream of the start of separation. This position was measured at two different x locations in the experiment, depending on the angle of attack: at $x = 2747.6$ mm for $\alpha = 5^\circ$, and at $x = 2757.6$ mm for $\alpha = -2.5^\circ$. In both cases, the y location was $y = -237.1$ mm, which was 1 mm from the fuselage. At these locations, the CFD somewhat overpredicted u velocity, but the v and w were well predicted. The $u'w'$, $v'v'$, and especially $u'u'$ were mispredicted, but the Reynolds stress components $v'w'$, $u'v'$, and $w'w'$ agreed well with experiment.

Comparisons are shown in Fig. 11 at the same chordwise location, but further from the corner at $y = -266.1$ mm (30 mm from the fuselage). This location was mostly outside of the fuselage boundary layer, which was roughly $20 - 30$ mm thick at this x station (it was thicker for $\alpha = -2.5^\circ$ than it was for $\alpha = 5^\circ$). All velocity components were predicted fairly well here. Also, the $u'u'$, $v'v'$, and $u'w'$ were reasonably well predicted in the outer part of the boundary layer, but were in error close to the wall. The $v'w'$, $u'v'$, and $w'w'$ were again all predicted reasonably close to experiment.

At a location closer to separation (which in the experiment was near to $x = 2850$ mm for $\alpha = 5^\circ$ and $x = 2885$ mm for $\alpha = -2.5^\circ$), the CFD suffered from too much sensitivity to grid density. Results are shown in Fig. 12 at the stations $x = 2822.6$ mm and $x = 2869.6$ mm, for the two angles of attack, respectively. In both cases, the y location was $y = -237.1$ mm, or 1 mm from the fuselage. As seen in Fig. 12(a) and (b), the computed CFD uncertainties were extremely large for the u and w components of velocity (although not shown, uncertainties for the Reynolds stresses were also very large). The reason for the large uncertainties is that the solution was changing significantly with increasing grid resolution, as shown in Fig. 12(c) and (d). In fact, at $\alpha = 5^\circ$, the C, M, and F grids all indicated separated flow already occurring prior to $x = 2822.6$ mm, while the XF grid yielded separation further downstream. At $\alpha = -2.5^\circ$, the C and M grids both indicated separated flow occurring prior to $x = 2869.6$ mm, while the F grid yielded incipient separation and the XF grid was attached. It appears that the CFD solutions on the F and XF grids were generally approaching the neighborhood of the experiment. However, the changes between the grid levels were still too large to be considered adequate for confident assessment of the results. A new set of refined grids (all in the same family) would be required to attain a better estimate of the CFD uncertainties here.

Figure 13 provides turbulence quantities at the same locations as the previous figure, showing only the F and XF grid results for clarity (the coarser grids not shown yielded very significant differences from these solutions). Here, it appears that the CFD computations using the SA-RC-QCR2013 model were again approaching the neighborhood of the experimental solutions as the grid was refined from F to XF. But these results also reinforce the fact that the current grids were too coarse for confident assessment of the results in this region.

Once the CFD is in error regarding the prediction of the separation location, then results downstream cannot be expected to agree with experiment. An example is shown in Fig. 14 for $\alpha = 5^\circ$, at the location $x = 2892.6$, $y = -246.1$ mm. This location is downstream of the start of separation in the experiment, 10 mm from the fuselage. CFD again predicted fairly large variations between the F and XF grid levels. The flow was more separated, and the turbulence peaks were predicted to be too high above the wing and generally much larger in magnitude than the experiment.

Figure 15 shows surface pressure coefficient comparisons for the $\alpha = 5^\circ$ case. Here, the experimental data includes 10 different runs, as well as data from both left and right wings, in order to give a feel for the experimental variability and uncertainty. Note that these experimental pressure data are *preliminary*, as they have not yet been fully analyzed. Overall, the CFD results agreed well with the experiment. In terms of grid convergence behavior, the stations near the wing root and wing tip exhibited grid sensitivity, with results changing between all grid levels. The finer grid results agreed better with the experiment at these locations. As discussed earlier, at the root, the finer grids yielded smaller junction separation. At the tip, the finer grids better resolved the wing tip vortex and its influence on the surface pressures.

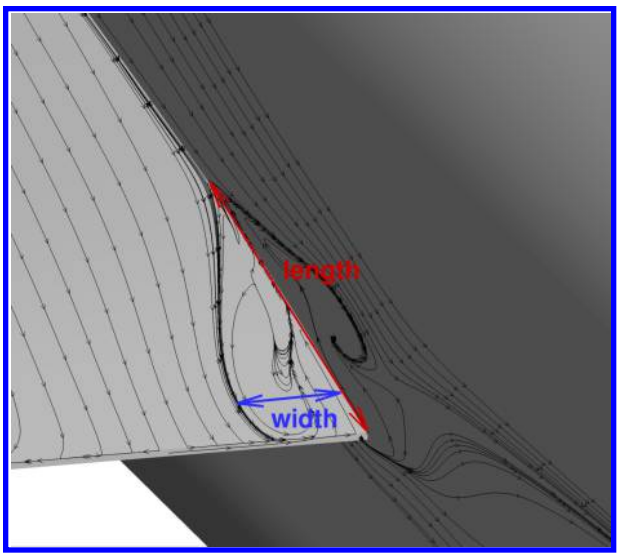

(a) Example separation at $\alpha = 5°$

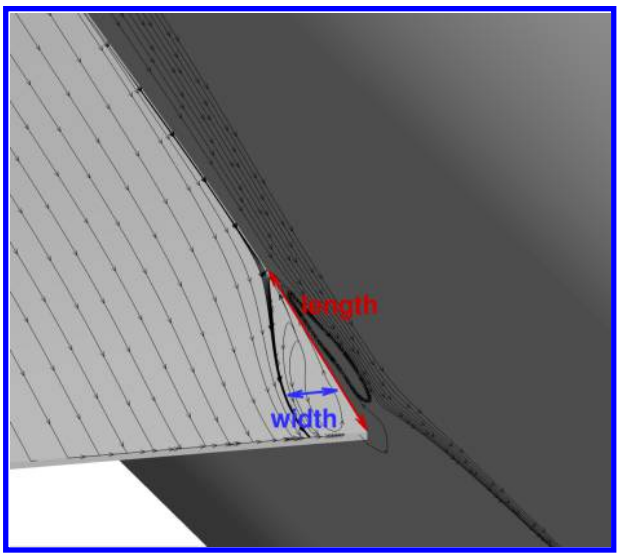

(b) Example separation at $\alpha = -2.5°$

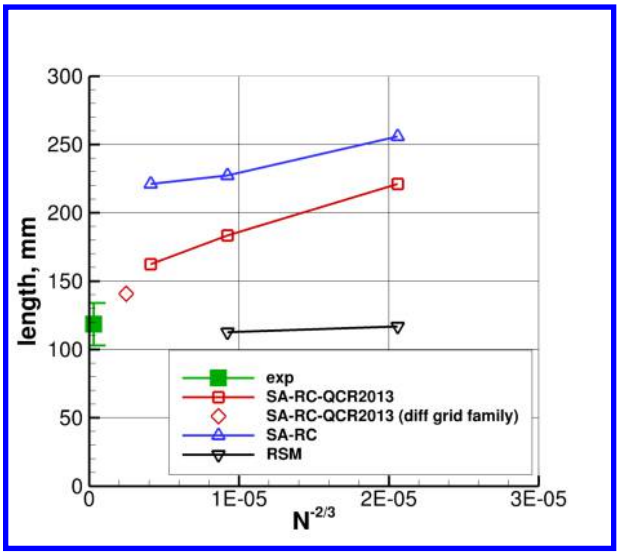

(c) Separation length at $\alpha = 5°$

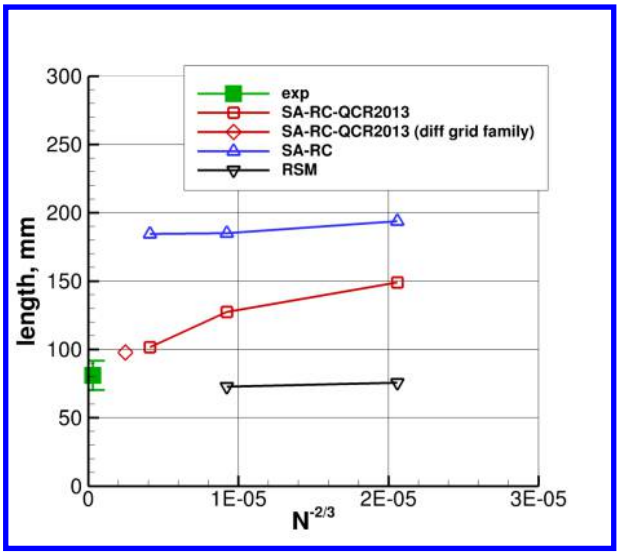

(d) Separation length at $\alpha = -2.5°$

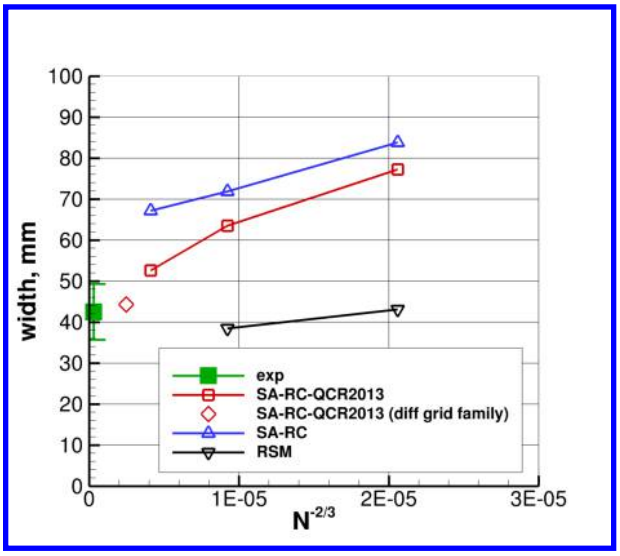

(e) Separation width at $\alpha = 5°$

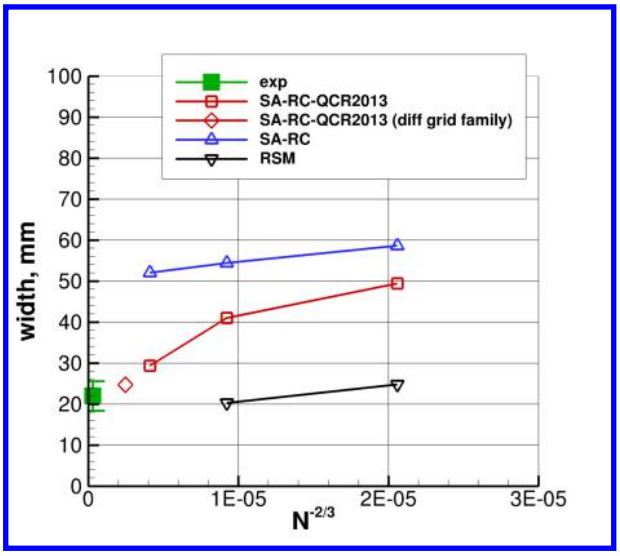

(f) Separation width at $\alpha = -2.5°$

Figure 4. Separation size as a function of grid density and turbulence model.

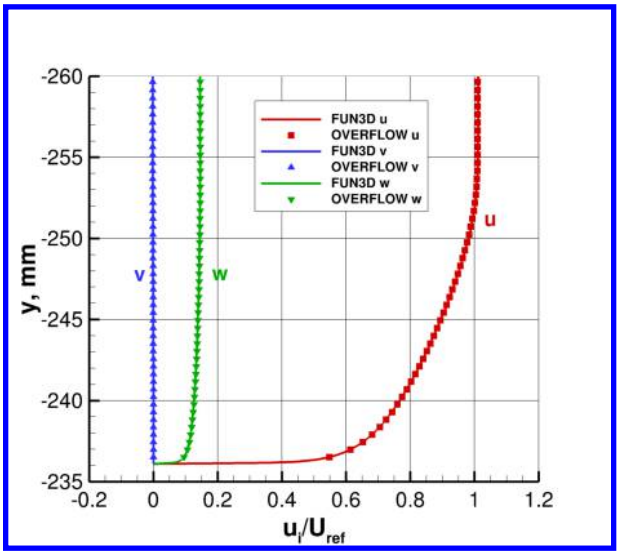

(a) Velocities at $\alpha = 5°$

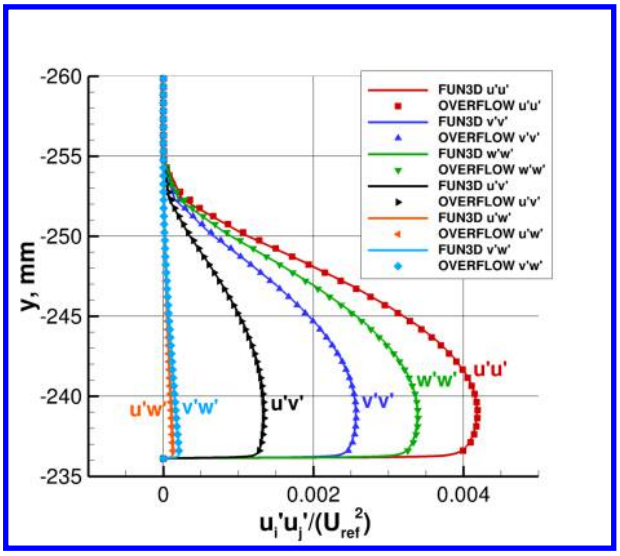

(b) Turbulence at $\alpha = 5°$

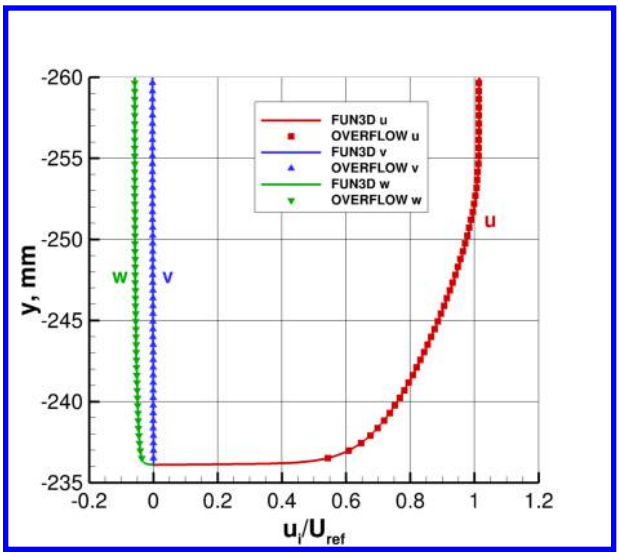

(c) Velocities at $\alpha = -2.5°$

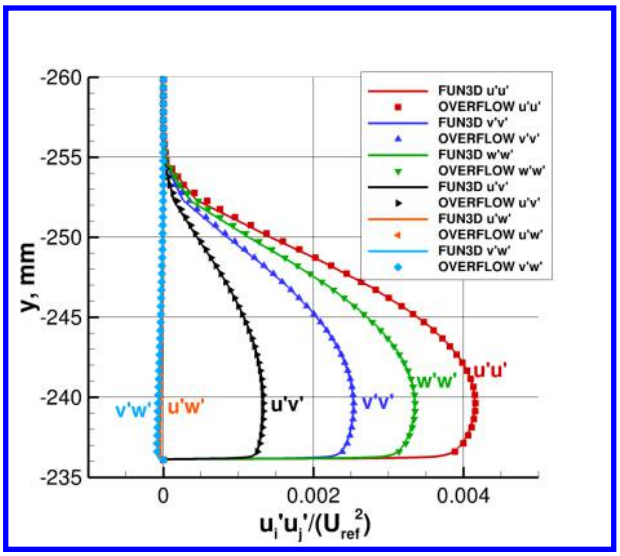

(d) Turbulence at $\alpha = -2.5°$

Figure 5. Comparison between FUN3D and OVERFLOW results using SA-RC-QCR2013, at $x = 1168.4$, $z = 0$ mm.

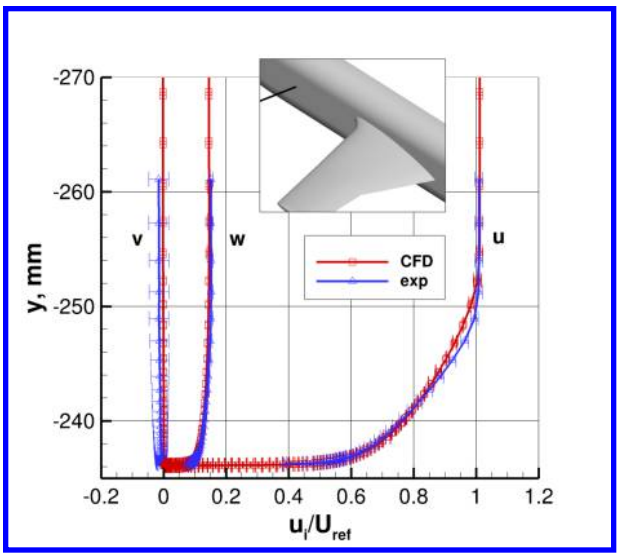

(a) Velocities at $\alpha = 5°$

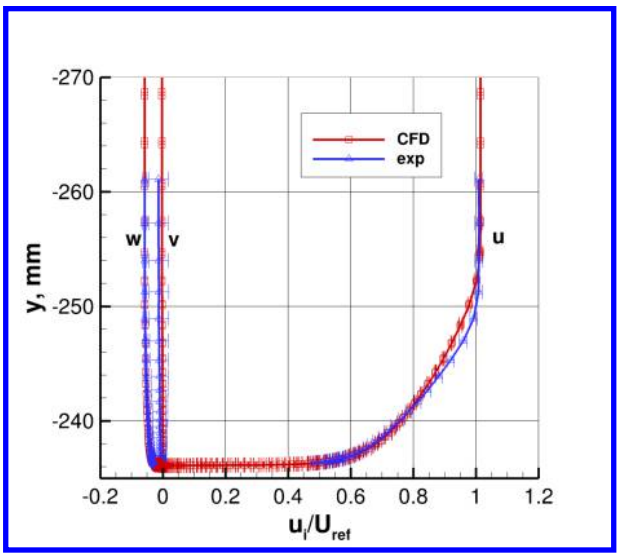

(b) Velocities at $\alpha = -2.5°$

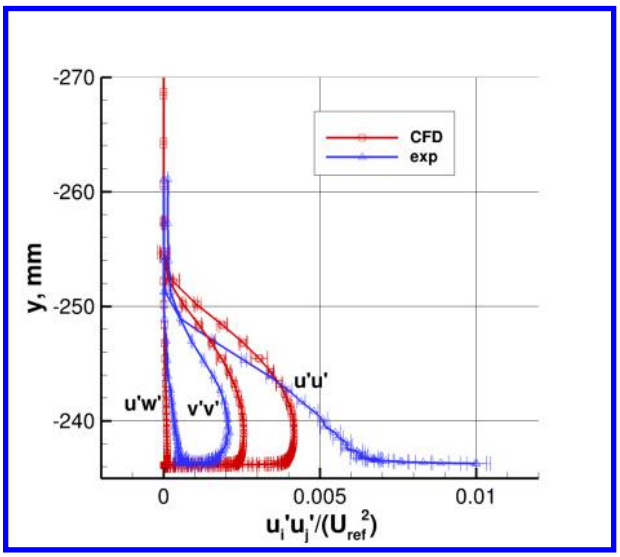

(c) Turbulence at $\alpha = 5°$, part 1

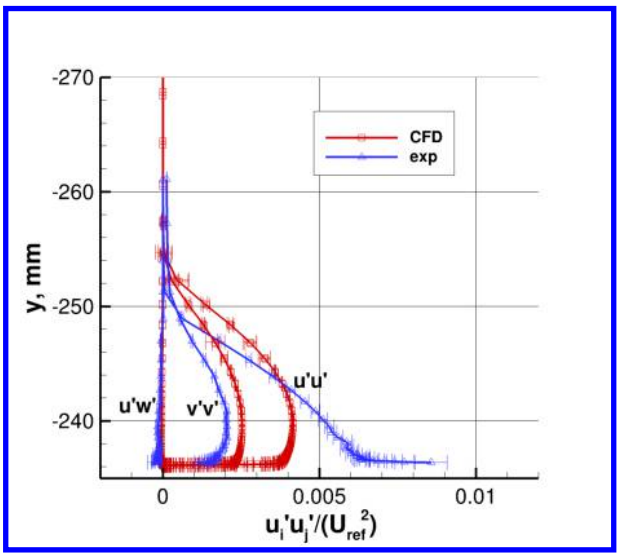

(d) Turbulence at $\alpha = -2.5°$, part 1

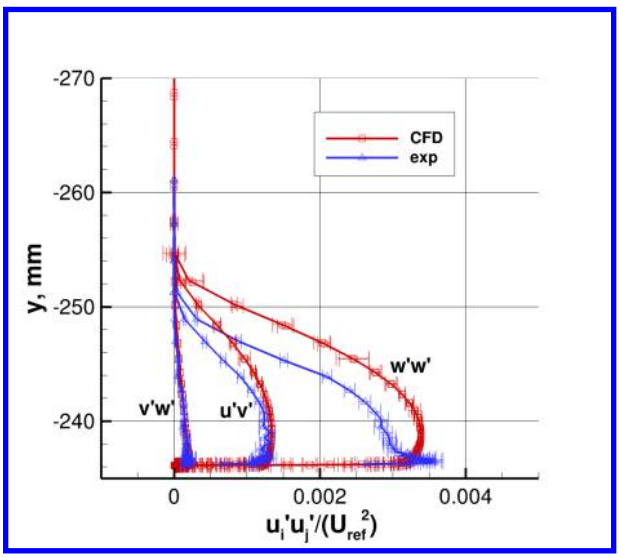

(e) Turbulence at $\alpha = 5°$, part 2

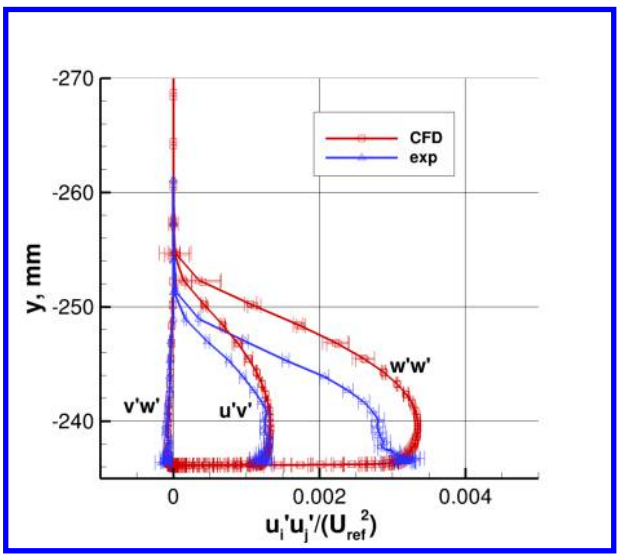

(f) Turbulence at $\alpha = -2.5°$, part 2

Figure 6. Comparison between CFD (using SA-RC-QCR2013 model) and experiment, including uncertainties, at $x = 1168.4$, $z = 0$ mm.

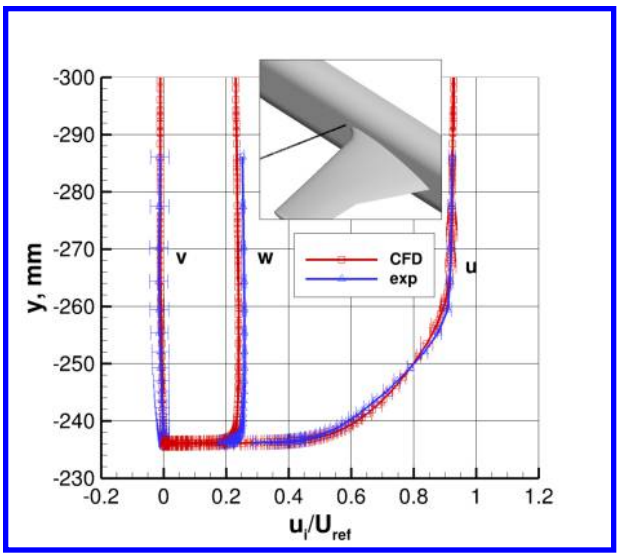

(a) Velocities at $\alpha = 5°$

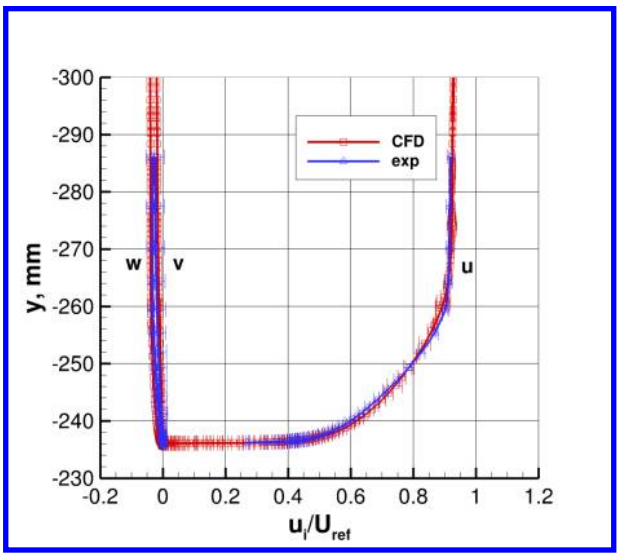

(b) Velocities at $\alpha = -2.5°$

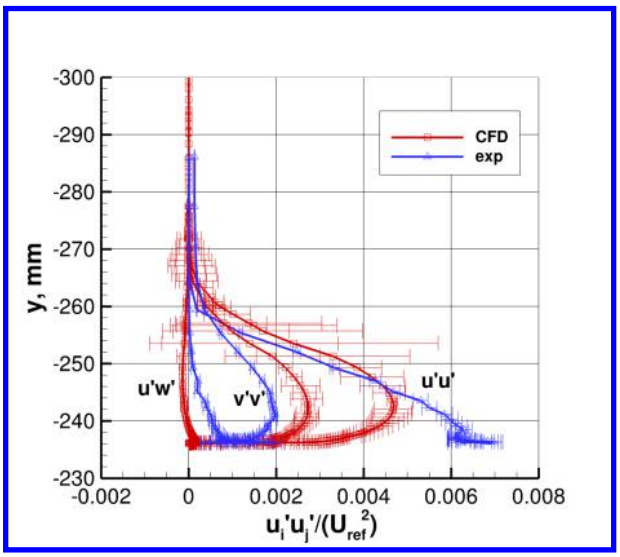

(c) Turbulence at $\alpha = 5°$, part 1

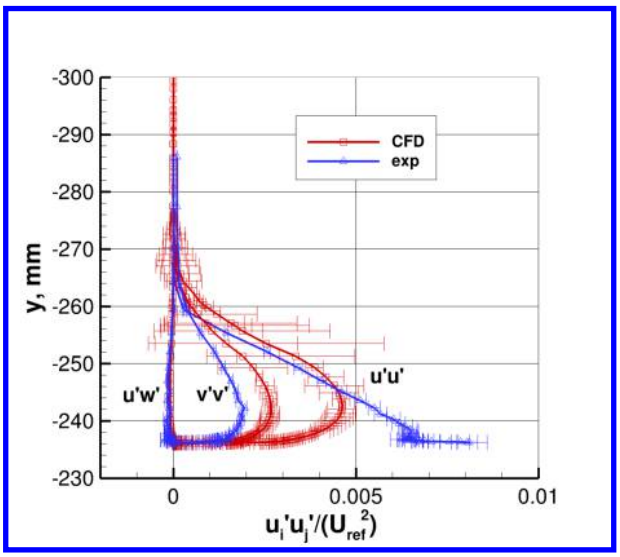

(d) Turbulence at $\alpha = -2.5°$, part 1

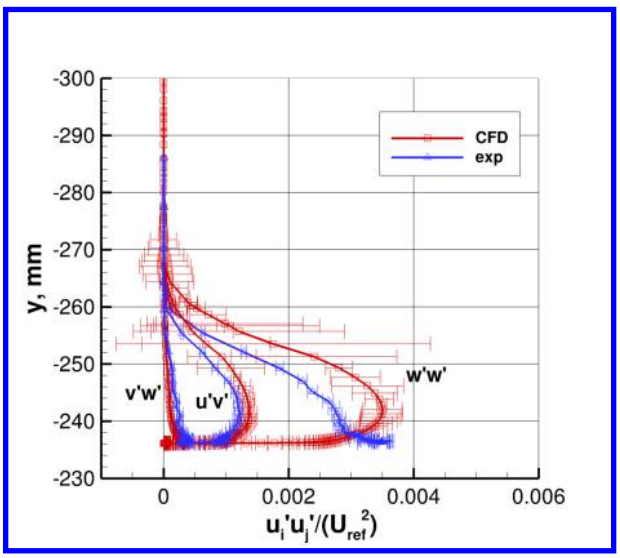

(e) Turbulence at $\alpha = 5°$, part 2

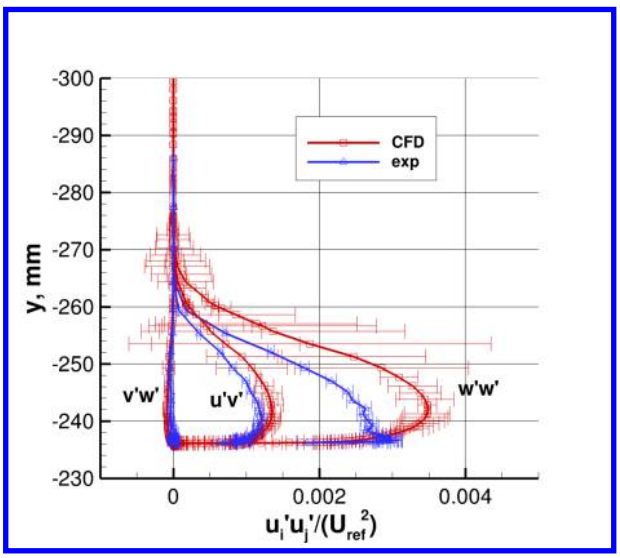

(f) Turbulence at $\alpha = -2.5°$, part 2

Figure 7. Comparison between CFD (using SA-RC-QCR2013 model) and experiment, including uncertainties, at $x = 1859.2$, $z = 55.05$ mm.

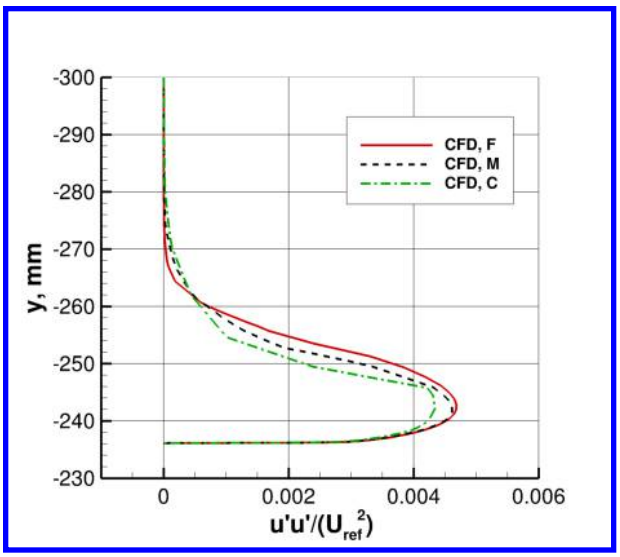

(a) $u'u'$

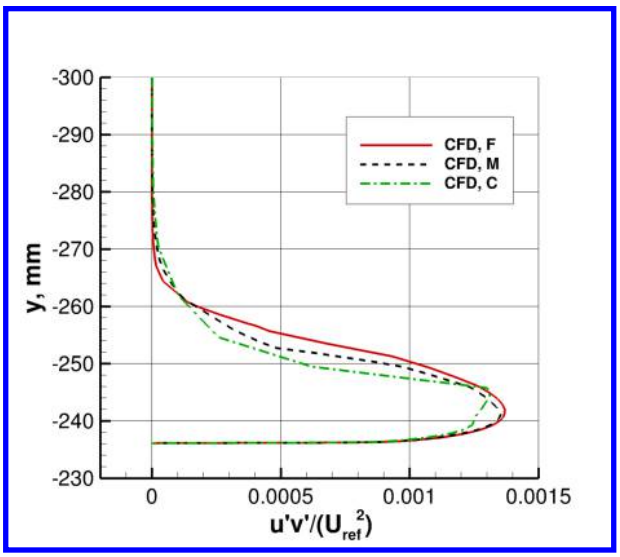

(b) $u'v'$

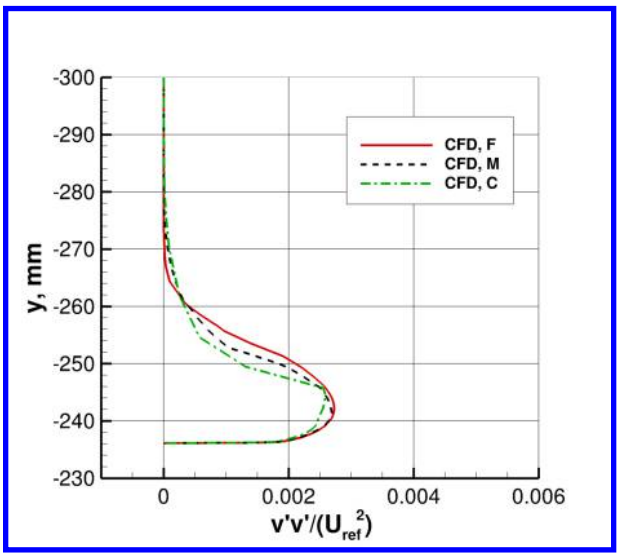

(c) $v'v'$

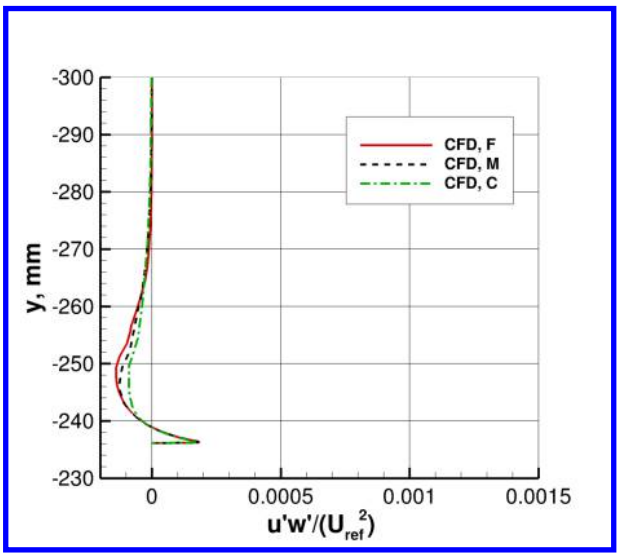

(d) $u'w'$

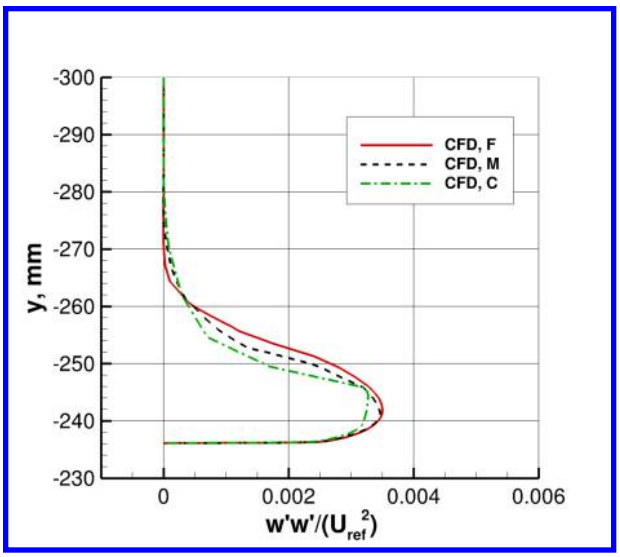

(e) $w'w'$

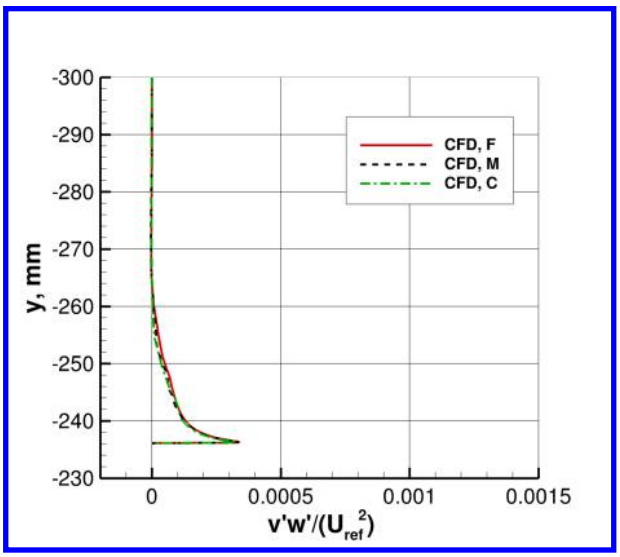

(f) $v'w'$

Figure 8. Reynolds stresses (using SA-RC-QCR2013 model) on all three grids for $\alpha = 5^\circ$ at $x = 1859.2$, $z = 55.05$ mm.

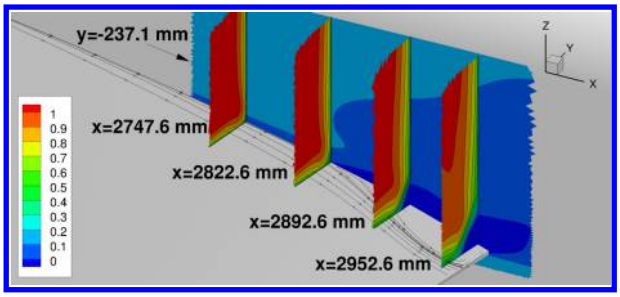

(a) u/U_{ref}

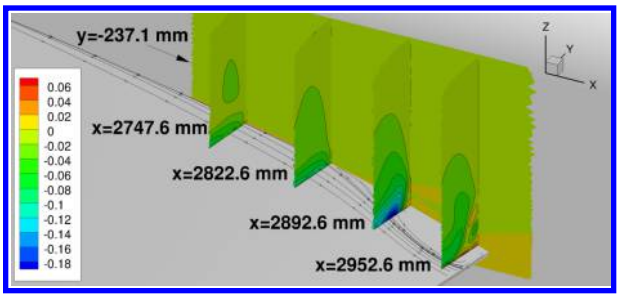

(b) v/U_{ref}

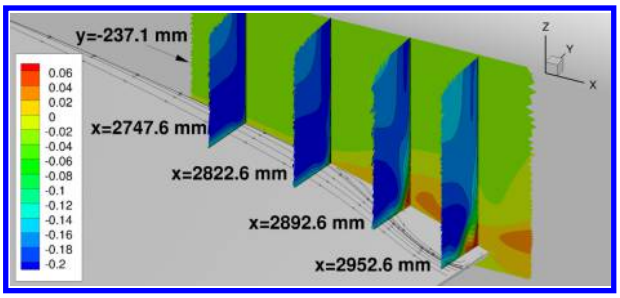

(c) w/U_{ref}

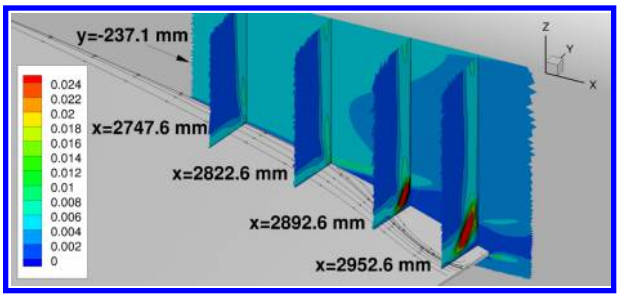

(d) $u'u'/(U_{ref}^2)$

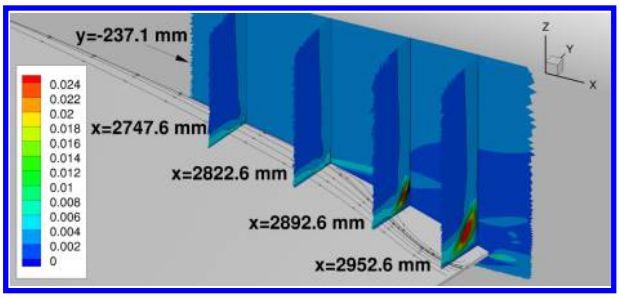

(e) $v'v'/(U_{ref}^2)$

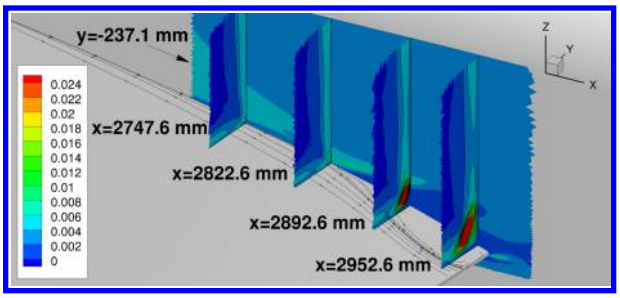

(f) $w'w'/(U_{ref}^2)$

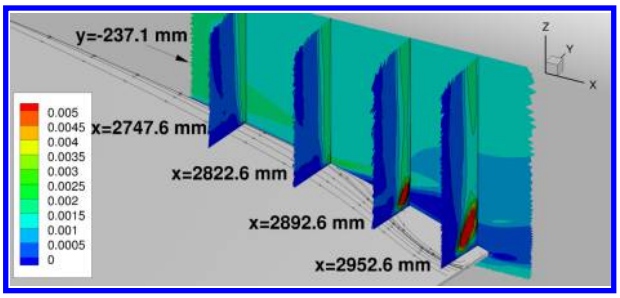

(g) $u'v'/(U_{ref}^2)$

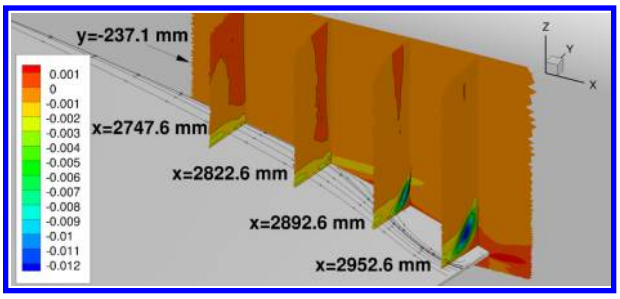

(h) $u'w'/(U_{ref}^2)$

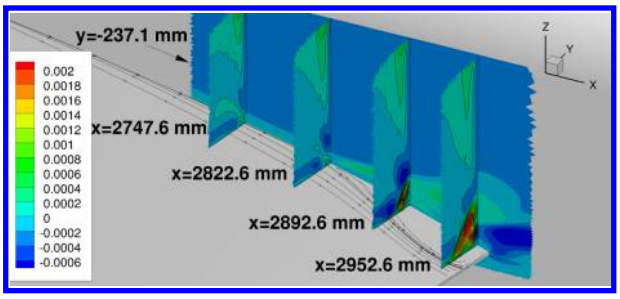

(i) $v'w'/(U_{ref}^2)$

Figure 9. Global view of velocities and Reynolds stresses in several planes near the trailing edge junction (using SA-RC-QCR2013 model), for $\alpha = 5°$.

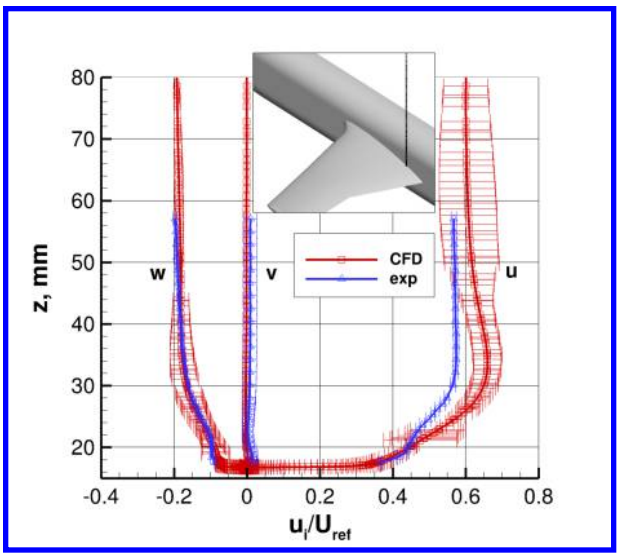

(a) Velocities at $\alpha = 5°$, $x = 2747.6$, $y = -237.1$ mm

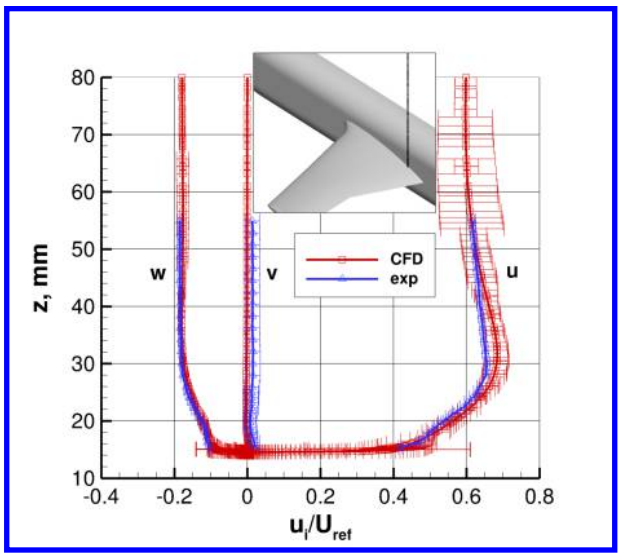

(b) Velocities at $\alpha = -2.5°$, $x = 2757.6$, $y = -237.1$ mm

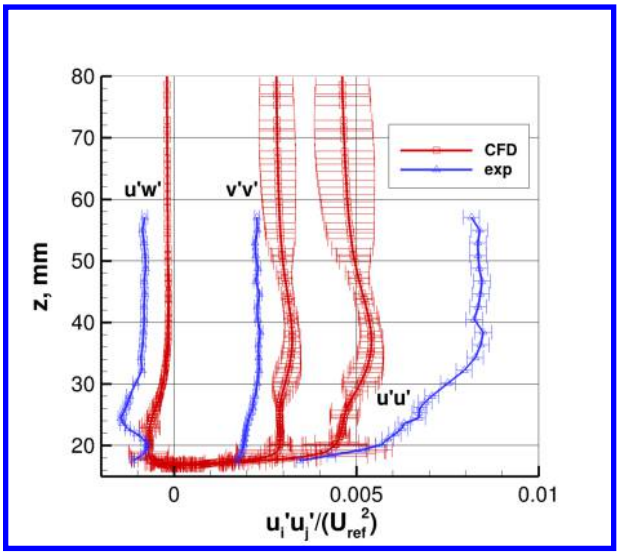

(c) Turbulence at $\alpha = 5°$, $x = 2747.6$, $y = -237.1$ mm, part 1

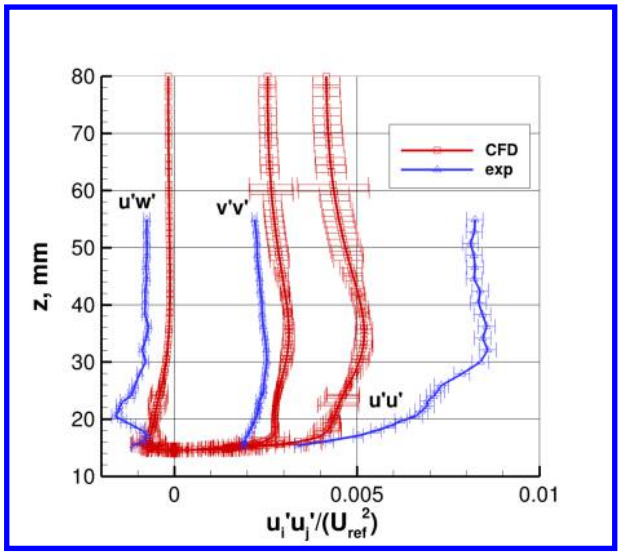

(d) Turbulence at $\alpha = -2.5°$, $x = 2757.6$, $y = -237.1$ mm, part 1

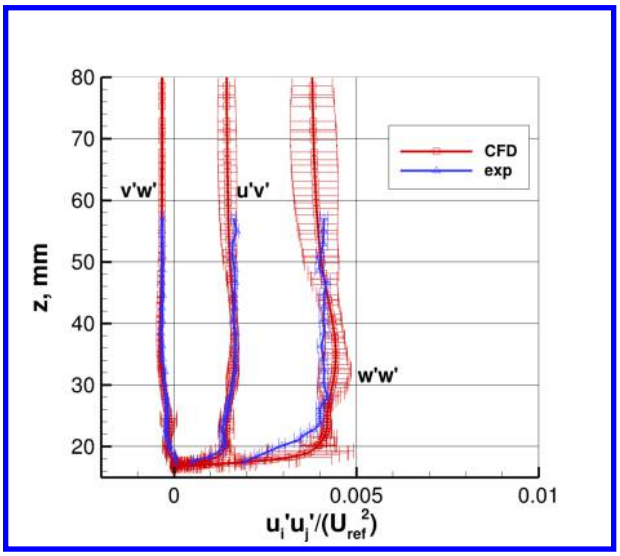

(e) Turbulence at $\alpha = 5°$, $x = 2747.6$, $y = -237.1$ mm, part 2

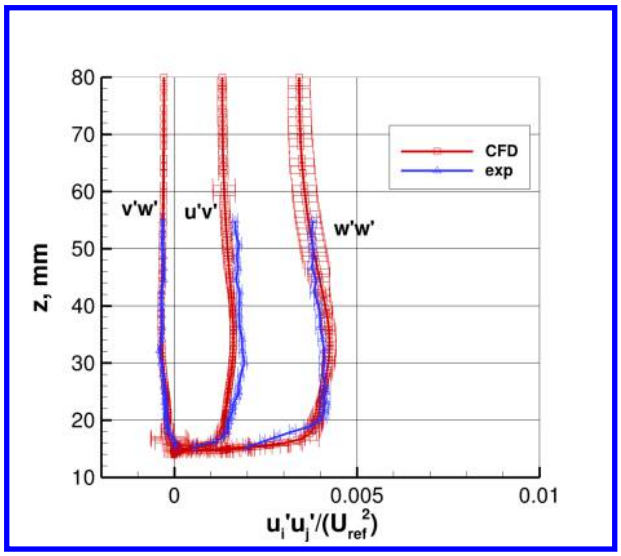

(f) Turbulence at $\alpha = -2.5°$, $x = 2757.6$, $y = -237.1$ mm, part 2

Figure 10. Comparison between CFD (using SA-RC-QCR2013 model) and experiment, including uncertainties, upstream of separation, 1 **mm from fuselage.**

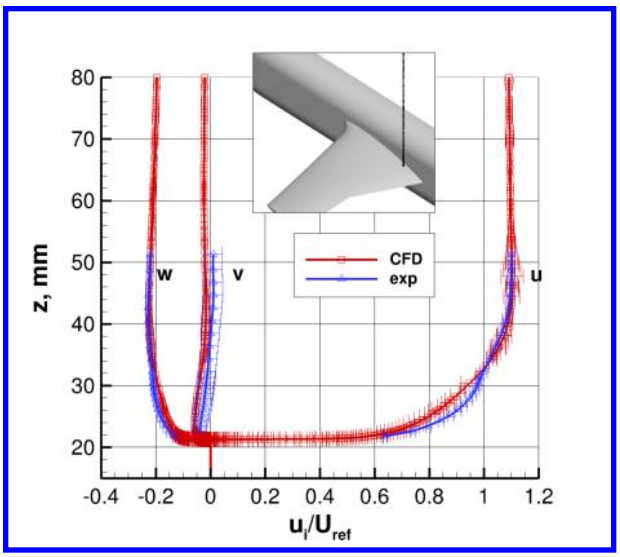

(a) Velocities at $\alpha = 5°$, $x = 2747.6$, $y = -266.1$ mm

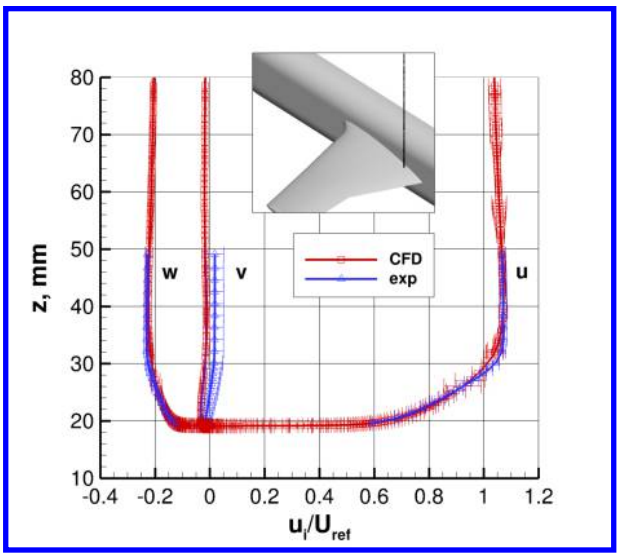

(b) Velocities at $\alpha = -2.5°$, $x = 2757.6$, $y = -266.1$ mm

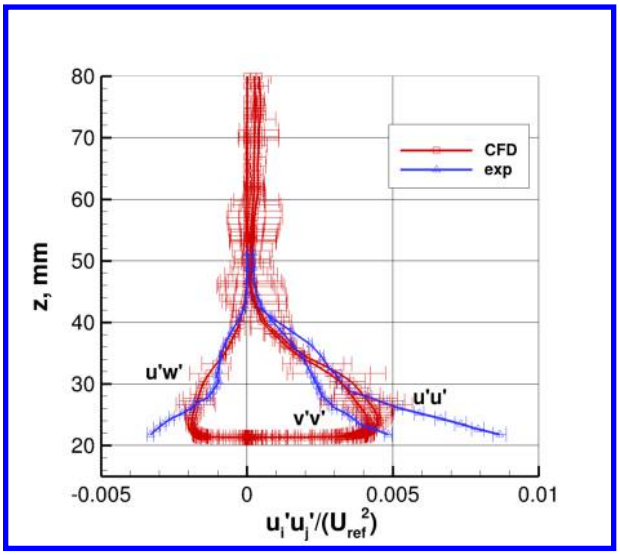

(c) Turbulence at $\alpha = 5°$, $x = 2747.6$, $y = -266.1$ mm, part 1

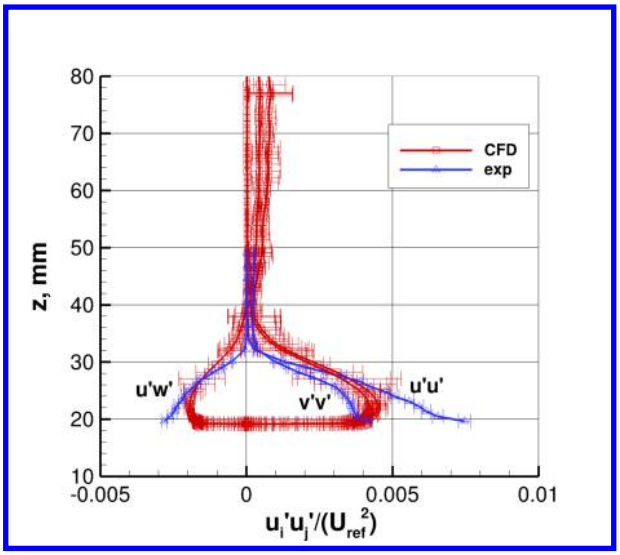

(d) Turbulence at $\alpha = -2.5°$, $x = 2757.6$, $y = -266.1$ mm, part 1

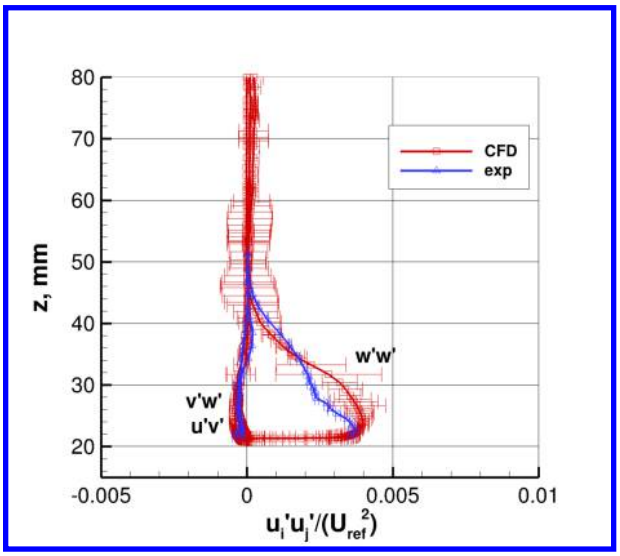

(e) Turbulence at $\alpha = 5°$, $x = 2747.6$, $y = -266.1$ mm, part 2

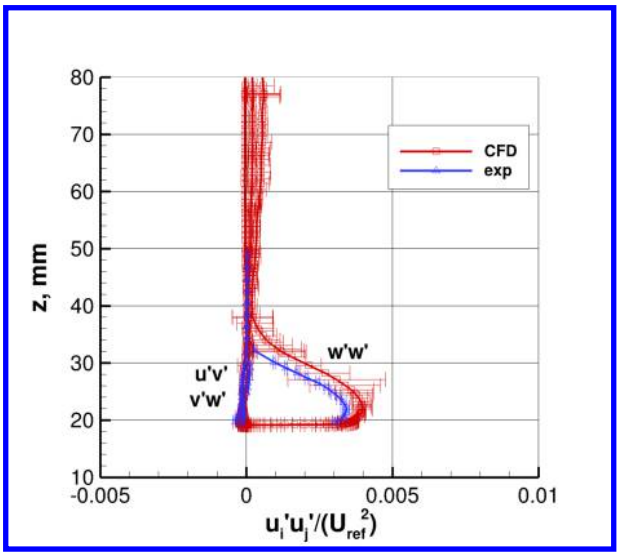

(f) Turbulence at $\alpha = -2.5°$, $x = 2757.6$, $y = -266.1$ mm, part 2

Figure 11. Comparison between CFD (using SA-RC-QCR2013 model) and experiment, including uncertainties, upstream of separation, 30 mm from fuselage.

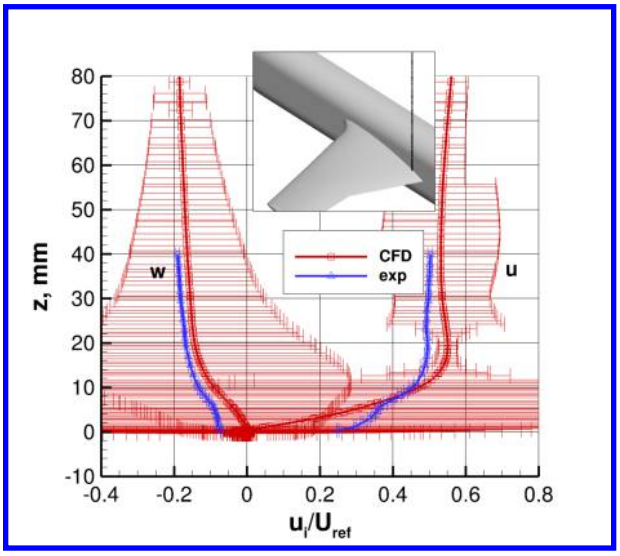

(a) Including uncertainties at $\alpha = 5°$, $x = 2822.6$, $y = -237.1$ mm

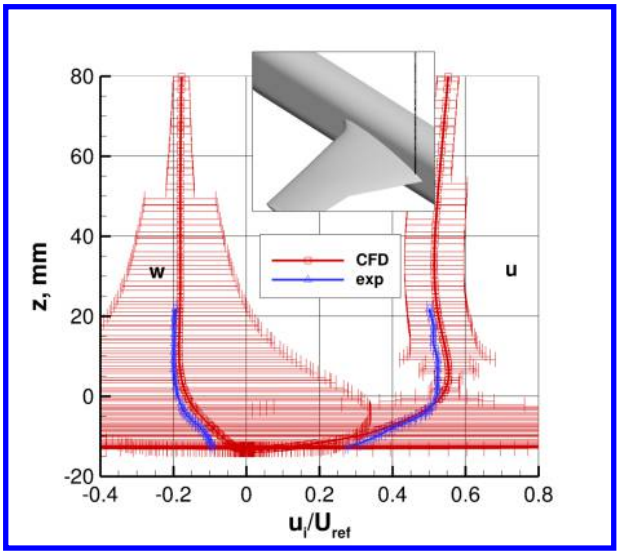

(b) Including uncertainties at $\alpha = -2.5°$, $x = 2869.6$, $y = -237.1$ mm

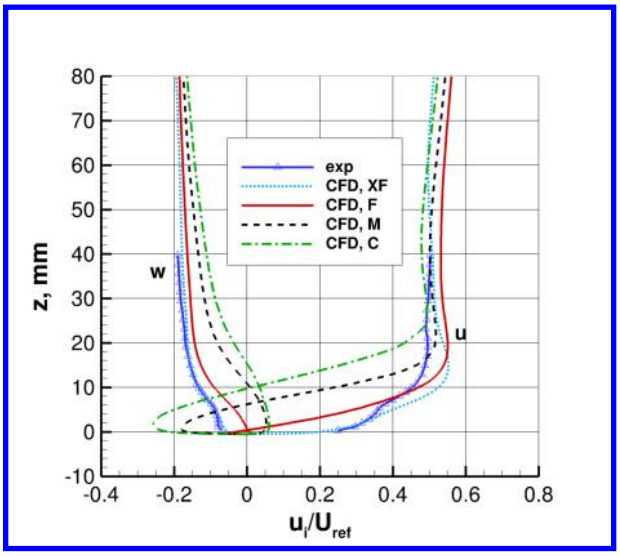

(c) All grids (including XF) at $\alpha = 5°$, $x = 2822.6$, $y = -237.1$ mm

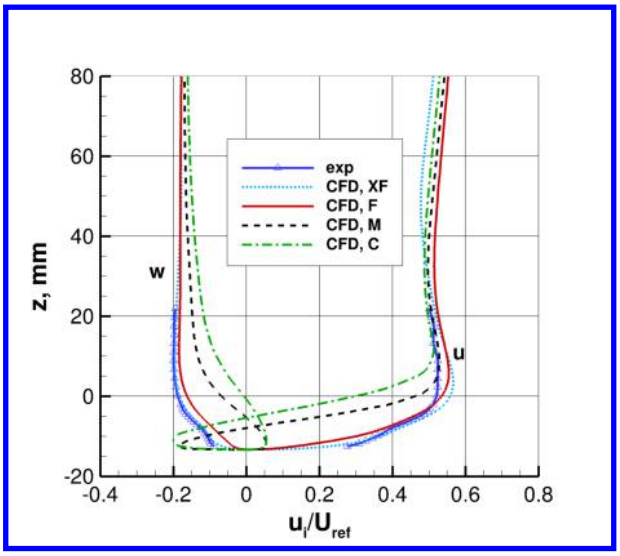

(d) All grids at $\alpha = -2.5°$, $x = 2869.6$, $y = -237.1$ mm

Figure 12. Comparison between CFD (using SA-RC-QCR2013 model) and experimental u and w velocities, close to start of separation, 1 mm from fuselage.

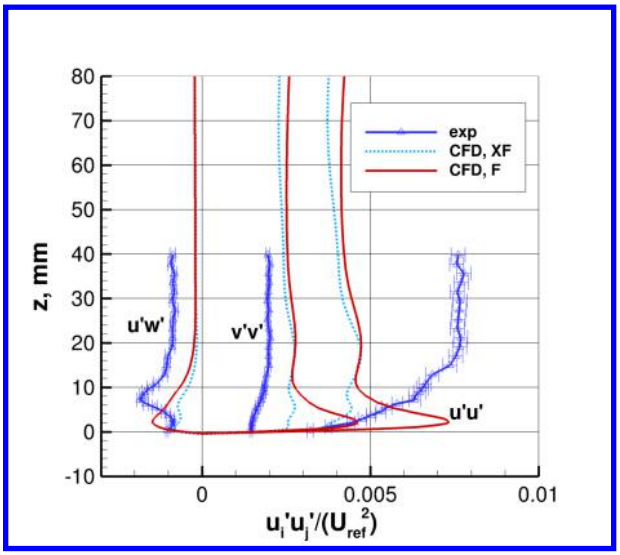

(a) F and XF grid results at $\alpha = 5°$, $x = 2822.6$, $y = -237.1$ mm, part 1

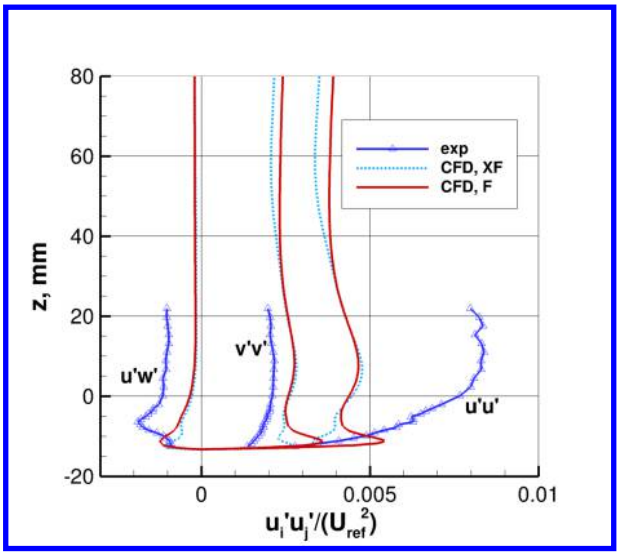

(b) F grid results at $\alpha = -2.5°$, $x = 2869.6$, $y = -237.1$ mm, part 1

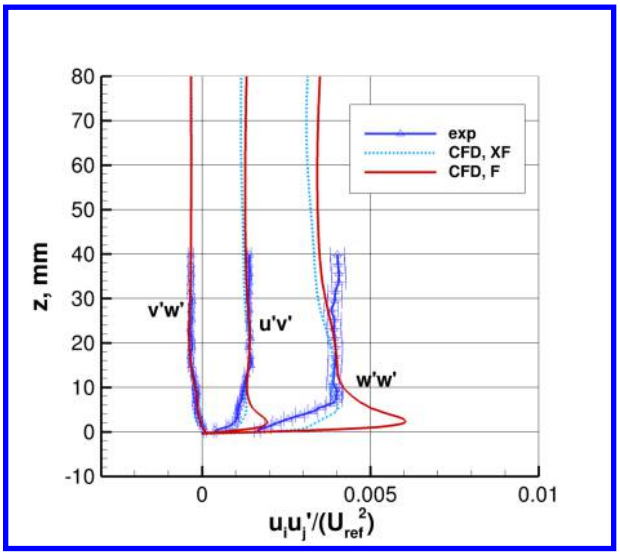

(c) F and XF grid results at $\alpha = 5°$, $x = 2822.6$, $y = -237.1$ mm, part 1

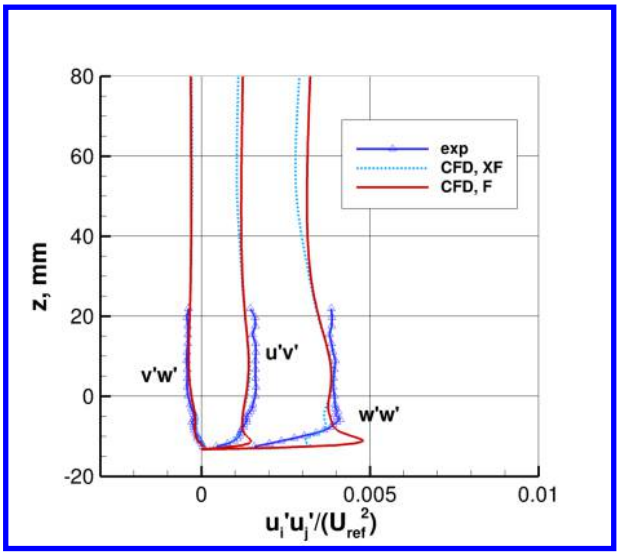

(d) F grid results at $\alpha = -2.5°$, $x = 2869.6$, $y = -237.1$ mm, part 1

Figure 13. Comparison between CFD (using SA-RC-QCR2013 model) and experimental Reynolds stresses, close to start of separation, 1 **mm from fuselage.**

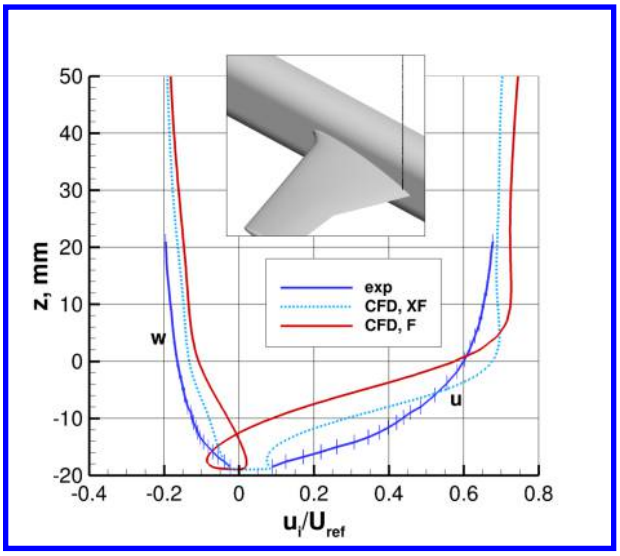

(a) Velocities

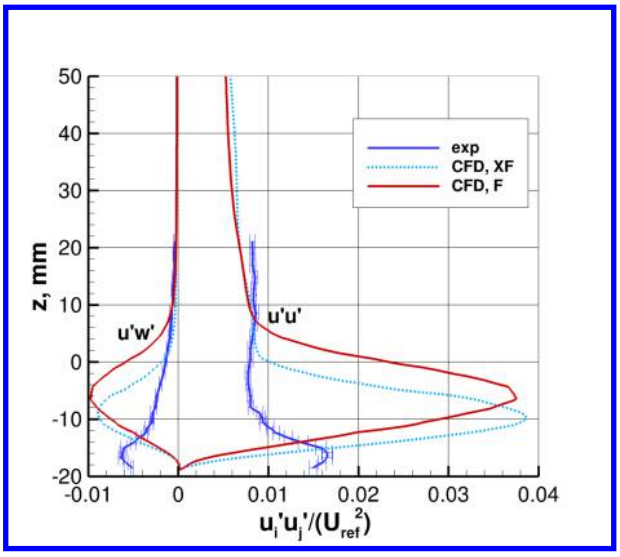

(b) Turbulence, part 1

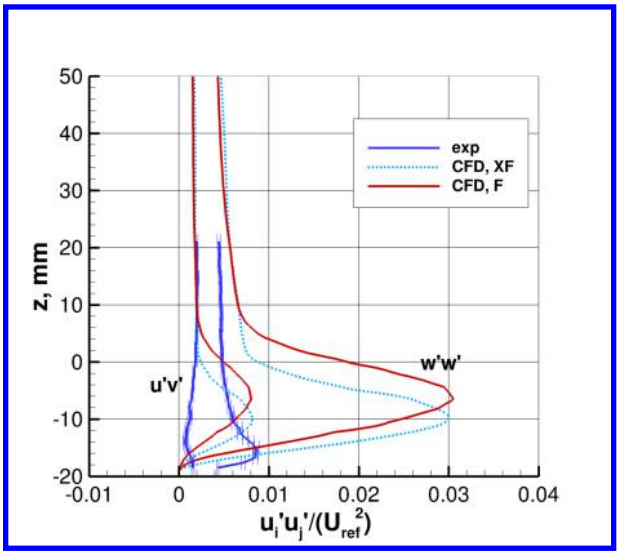

(c) Turbulence, part 2

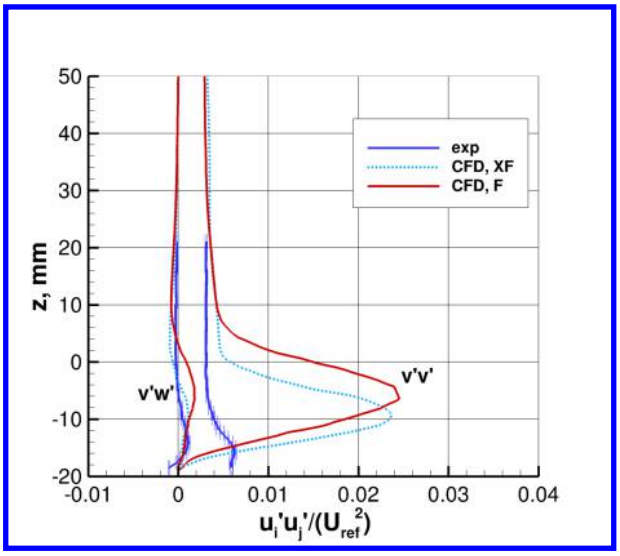

(d) Turbulence, part 3

Figure 14. Comparisons between CFD (using SA-RC-QCR2013 model on F and XF grids) and experiment at $\alpha = 5^\circ$ downstream of separation, $x = 2892.6$, $y = -246.1$ mm.

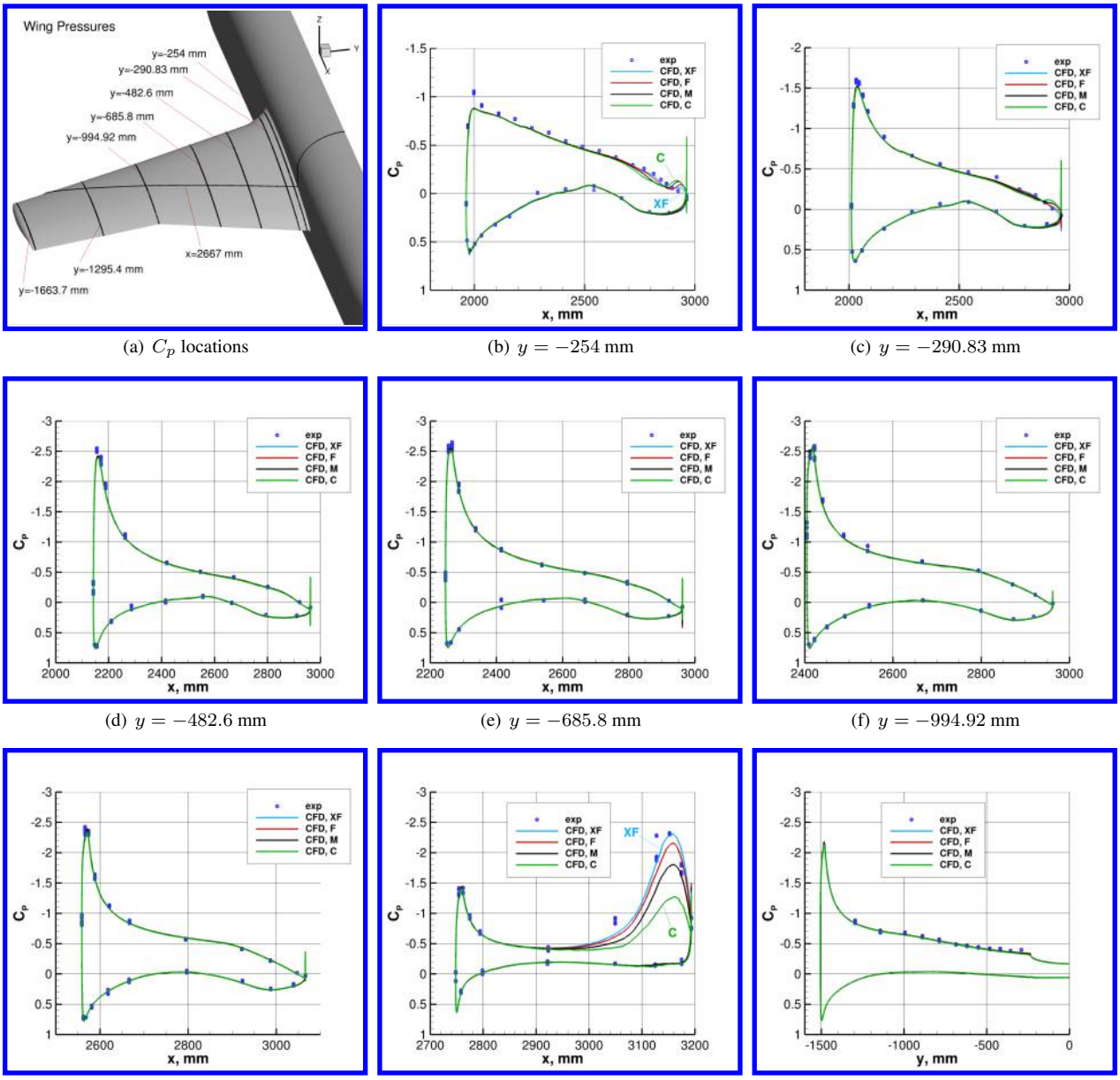

(a) C_p locations (b) $y = -254$ mm (c) $y = -290.83$ mm

(d) $y = -482.6$ mm (e) $y = -685.8$ mm (f) $y = -994.92$ mm

(g) $y = -1295.4$ mm (h) $y = -1663.7$ mm (i) $x = 2667$ mm

Figure 15. Comparison of computed wing surface pressure coefficients (using SA-RC-QCR2013 model) with experiment at $\alpha = 5°$.

E. Effect of Turbulence Model

As already noted, three different turbulence models have been employed to date in this study: SA-RC-QCR2013, SA-RC, and RSM. Overall results with these models were shown in Fig. 4. Recall that the SA-RC-QCR2013 and RSM models both yielded separation sizes that best matched experiment, while the SA-RC model predicted too large a separation size. However, SA-RC and RSM were only run on the C and M grids. Here, we directly compare detailed flowfield results from the three models on the M grid. Because the grid size has been shown to have a big effect on the results near separation, these comparisons on the M grid should be viewed with caution.

Figure 16 compares quantities upstream of separation, 1 mm from the fuselage. In terms of velocity, the SA-RC model missed the profile very close to the wall, while the other two models were closer. Without QCR2013, the SA-RC model predicted little difference between the normal Reynolds stresses ($u'u'$, $v'v'$, and $w'w'$), while SA-RC-QCR2013 and RSM both yielded results similar to each other, and were somewhat closer to experiment. All three models missed $u'w'$ similarly, and all predicted $u'v'$ and $u'w'$ fairly close to each other and to experiment.

Comparisons are shown at the same x stations, 30 mm from the fuselage, in Fig. 17. The RSM in this case yielded better velocity profiles in comparison with experiment for the $\alpha = 5^\circ$ case. In terms of the turbulence, all three models were fairly similar to each other (although SA-RC again did not predict as much differences between the normal Reynolds stresses as the other models, as expected).

Results close to the start of separation (1 mm from the fuselage) are shown in Fig. 18. Here, recall that the SA-RC-QCR2013 model showed very large sensitivities to grid density. On the M level, this model produced separated flow at this location (while results on finer grids tended toward more attached flow). SA-RC results on the M grid were even more separated than SA-RC-QCR2013, while RSM produced velocity profiles in very good agreement with experiment. The RSM turbulence results also generally agreed better with experiment overall, although there were clearly some deviations from experiment for $u'u'$, $w'w'$, and $u'w'$.

Overall, on the M grid, the RSM tended to perform the best of the three models and SA-RC the worst. However, the SA-RC-QCR2013 results appeared to come very close to the experiment as the grid was refined. Results on the full suite of C-M-F-XF grids would be required to fully assess the grid sensitivity of all models. For example, we do not know if the RSM will predict *too small* a separation as the grid is refined, or if its trend of minimal grid sensitivity will hold. To date, the implementation of RSM in FUN3D has exhibited robustness issues (failure to converge) on the finer grids tested.

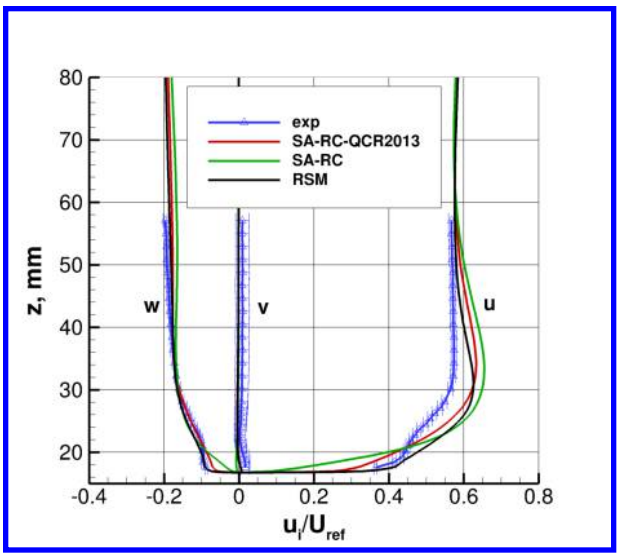

(a) Velocities at $\alpha = 5°$, $x = 2747.6$, $y = -237.1$ mm

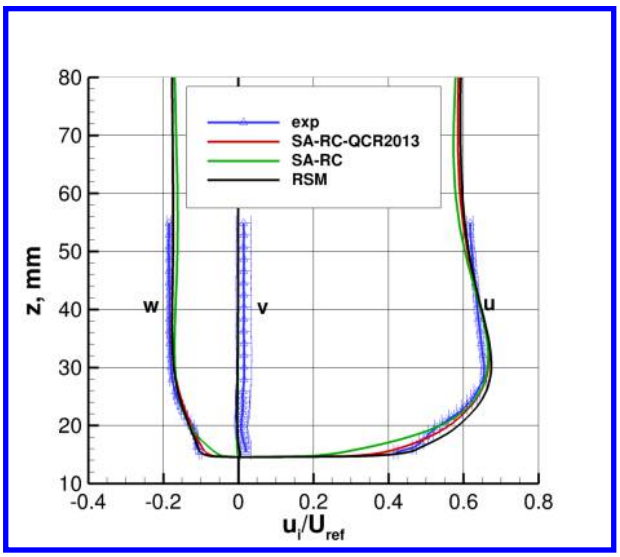

(b) Velocities at $\alpha = -2.5°$, $x = 2757.6$, $y = -237.1$ mm

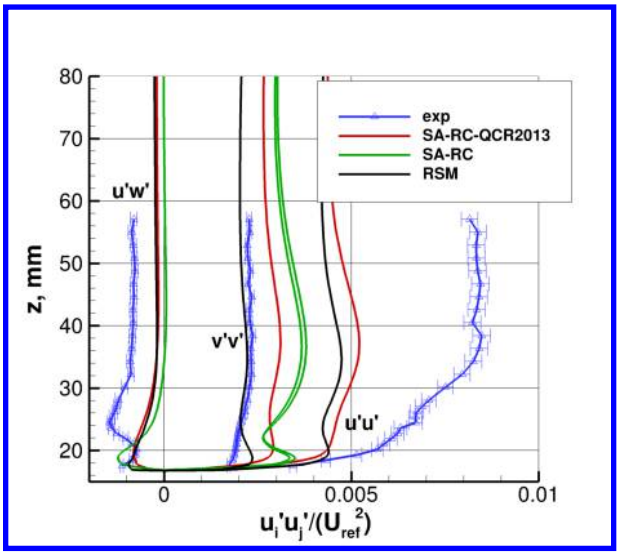

(c) Turbulence at $\alpha = 5°$, $x = 2747.6$, $y = -237.1$ mm, part 1

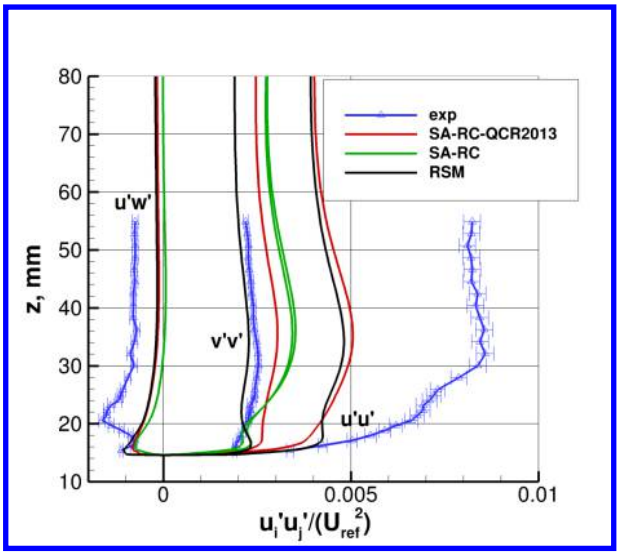

(d) Turbulence at $\alpha = -2.5°$, $x = 2757.6$, $y = -237.1$ mm, part 1

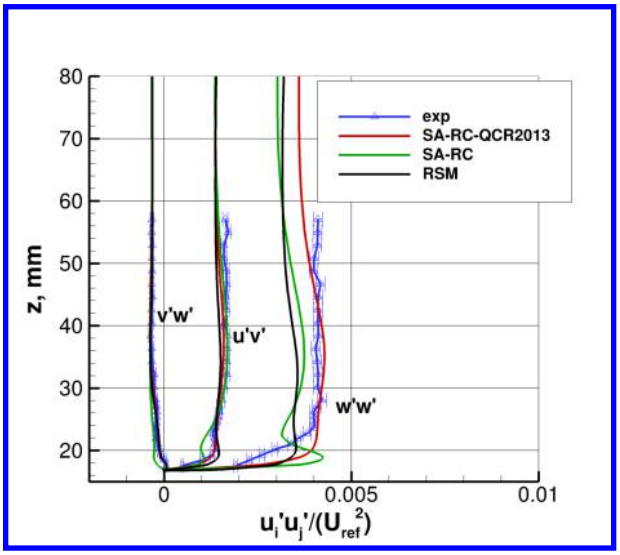

(e) Turbulence at $\alpha = 5°$, $x = 2747.6$, $y = -237.1$ mm, part 2

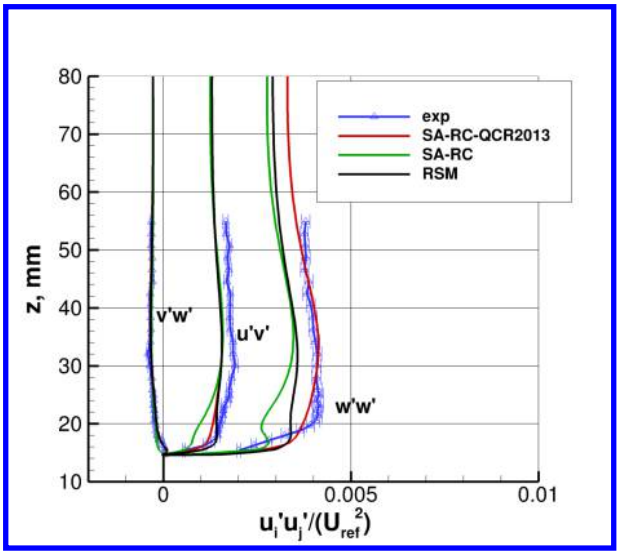

(f) Turbulence at $\alpha = -2.5°$, $x = 2757.6$, $y = -237.1$ mm, part 2

Figure 16. Comparison between turbulence models on M grid, upstream of separation, 1 mm from fuselage.

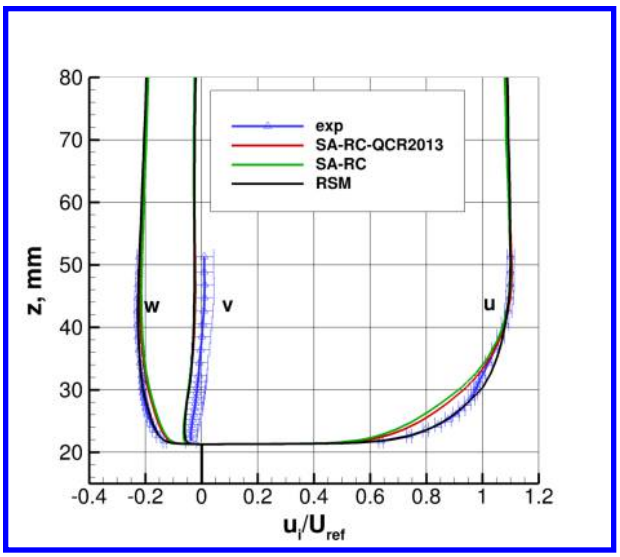

(a) Velocities at $\alpha = 5°$, $x = 2747.6$, $y = -266.1$ mm

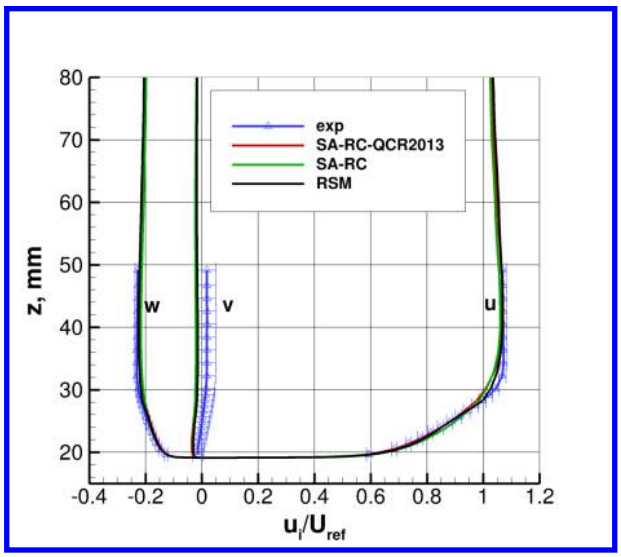

(b) Velocities at $\alpha = -2.5°$, $x = 2757.6$, $y = -266.1$ mm

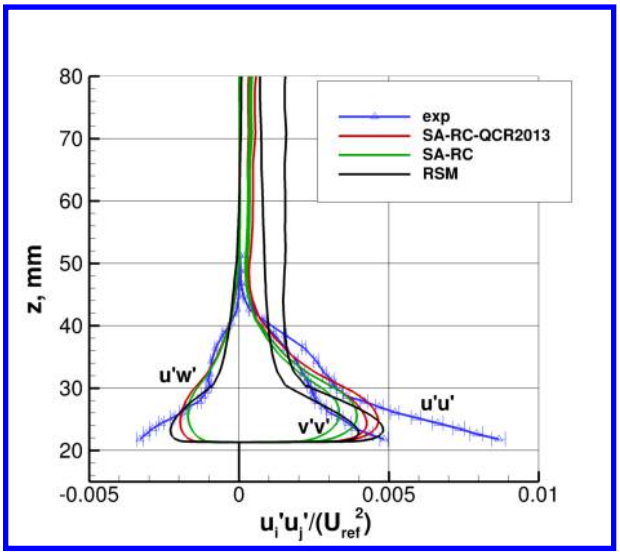

(c) Turbulence at $\alpha = 5°$, $x = 2747.6$, $y = -266.1$ mm, part 1

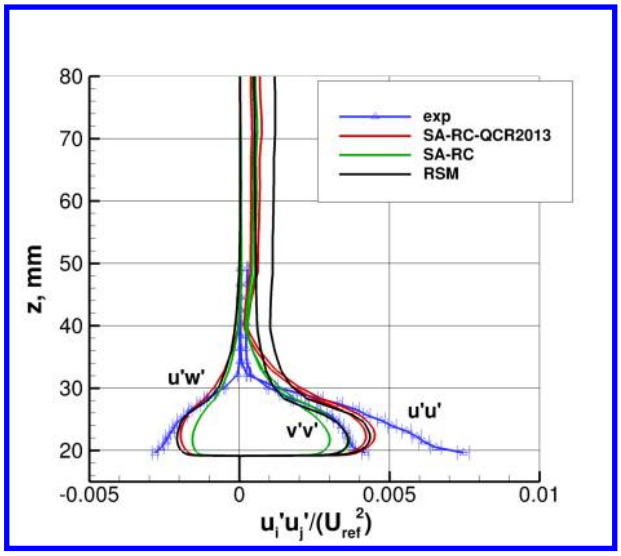

(d) Turbulence at $\alpha = -2.5°$, $x = 2757.6$, $y = -266.1$ mm, part 1

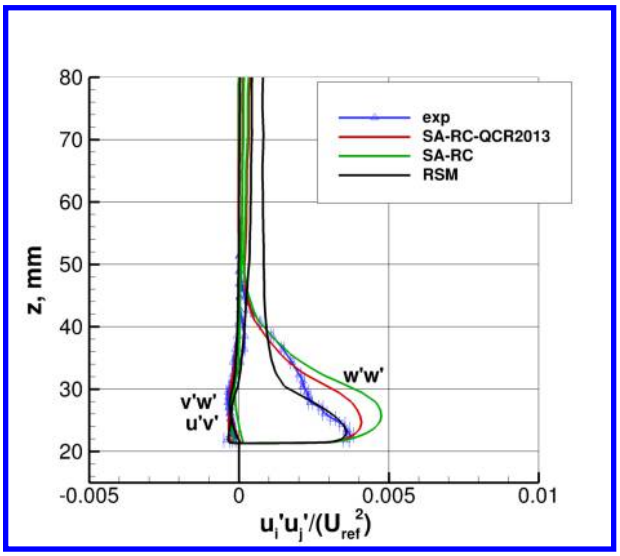

(e) Turbulence at $\alpha = 5°$, $x = 2747.6$, $y = -266.1$ mm, part 2

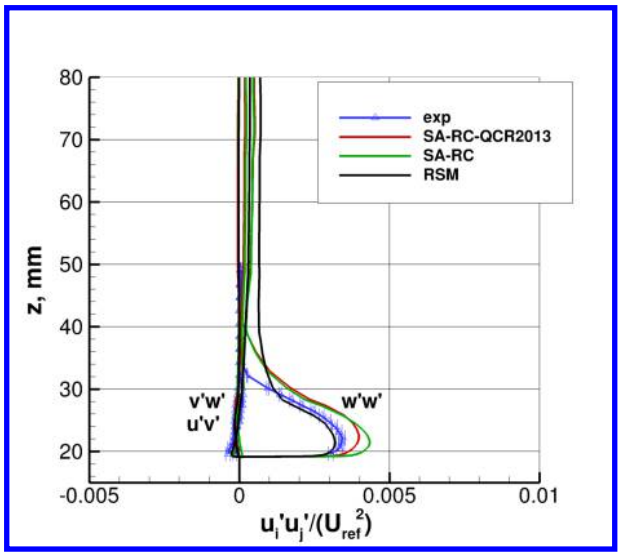

(f) Turbulence at $\alpha = -2.5°$, $x = 2757.6$, $y = -266.1$ mm, part 2

Figure 17. Comparison between turbulence models on M grid, upstream of separation, 30 mm from fuselage.

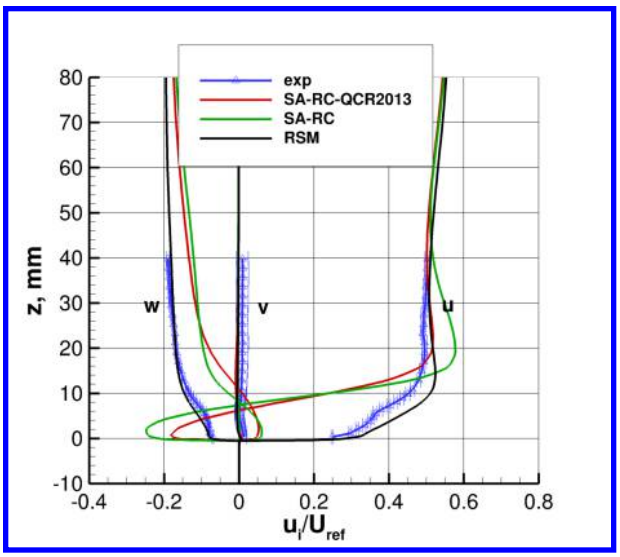

(a) Velocities at $\alpha = 5°$, $x = 2822.6$, $y = -237.1$ mm

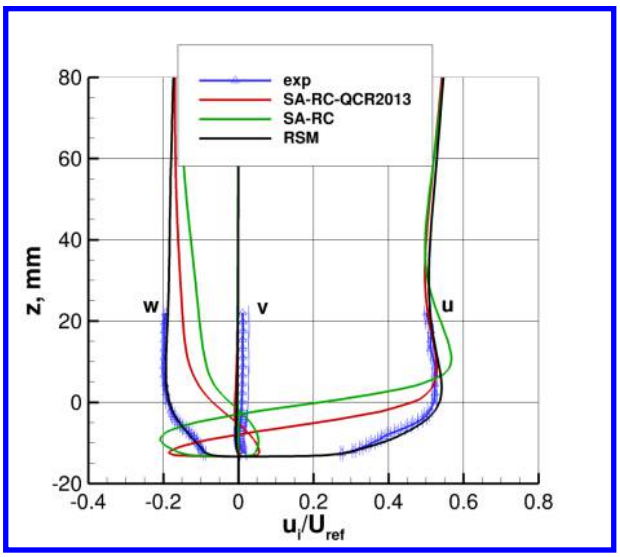

(b) Velocities at $\alpha = -2.5°$, $x = 2869.6$, $y = -237.1$ mm

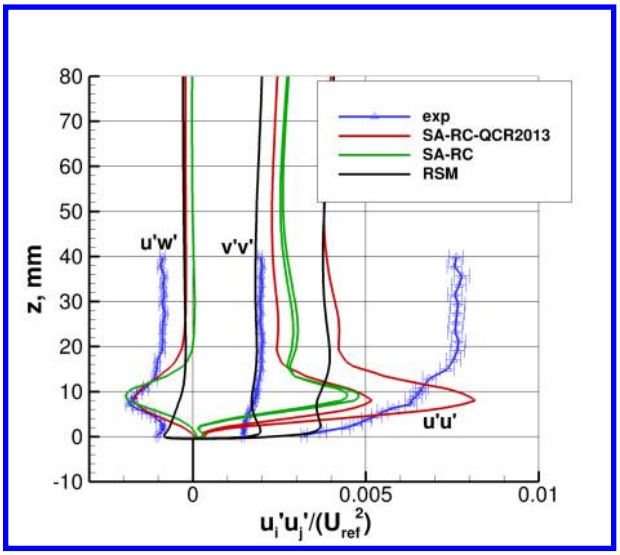

(c) Turbulence at $\alpha = 5°$, $x = 2822.6$, $y = -237.1$ mm, part 1

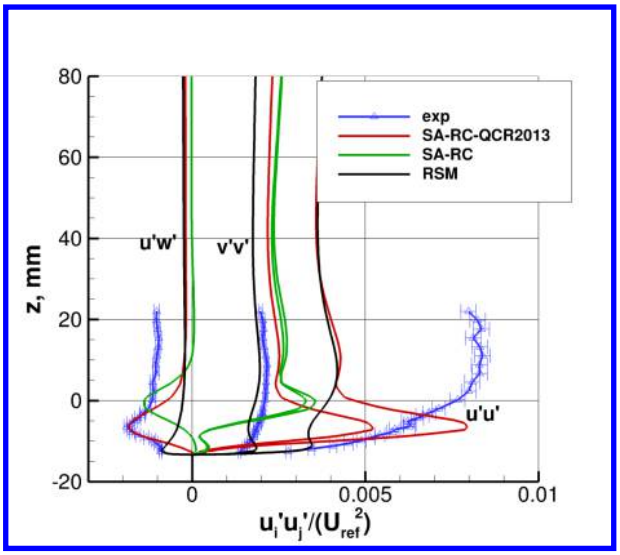

(d) Turbulence at $\alpha = -2.5°$, $x = 2869.6$, $y = -237.1$ mm, part 1

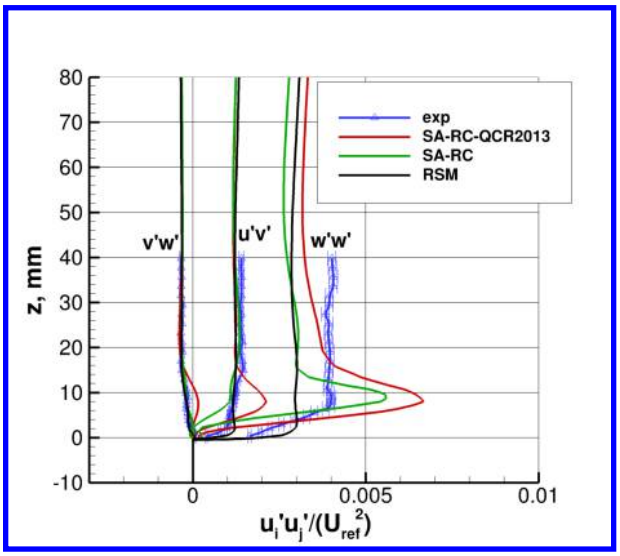

(e) Turbulence at $\alpha = 5°$, $x = 2822.6$, $y = -237.1$ mm, part 2

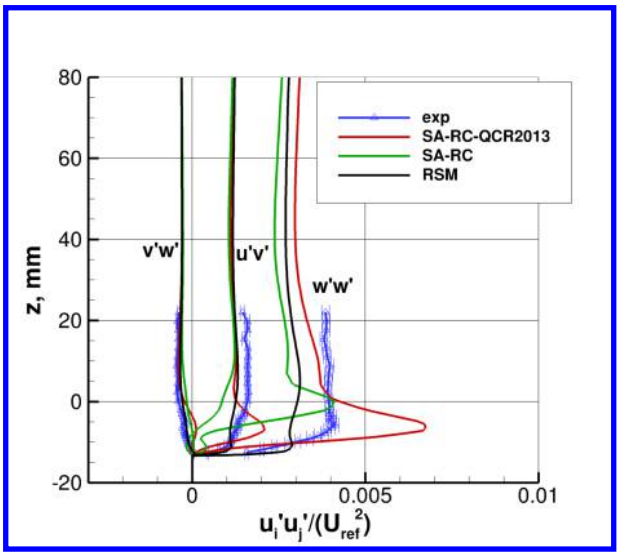

(f) Turbulence at $\alpha = -2.5°$, $x = 2869.6$, $y = -237.1$ mm, part 2

Figure 18. Comparison between turbulence models on M grid, close to start of separation, 1 mm from fuselage.

VI. Conclusions

A preliminary study was performed comparing CFD with experimental data for the NASA Juncture Flow configuration. This recent experiment measured detailed flowfield data in the wing-body junction (corner) region near the wing trailing edge where separation occurs. Although future CFD results will include the wind tunnel walls, the current study only used free-air grids. Two angles of attack were considered, based on the incidence angles in the tunnel (no corrections were applied to the free-air computations). The main purpose was to try to determine overall grid sensitivity and gridding needs, as well as to get a preliminary look at how well (or poorly) today's state-of-the-art RANS turbulence models perform.

The SA-RC model predicted separation to be too large, whereas SA-RC-QCR2013 and RSM both predicted results in line with experiment. However, SA-RC-QCR2013 was very sensitive to the grid density, with coarser grids predicting too much separation and finer grids approaching similar separation size to experiment. The RSM on coarser grids agreed reasonably well with experimental separation size, but the model could not be successfully run on the finer grids. This lack of robustness is often encountered with full second-moment seven-equation Reynolds stress models; it leaves a big hole in the current study. For example, it is not known whether the grid-converged RSM results approach experiment (like SA-RC-QCR2013), or whether its results trend toward separation sizes that are too small.

Surface pressure comparisons between CFD and (preliminary) experiment appeared to be reasonable. Besides the separated junction region, the wing tip region also exhibited significant sensitivity of surface pressures to grid density. Comparisons of velocity profiles and Reynolds stresses showed general consistency upstream of separation, with the biggest differences between CFD and experiment typically occurring in the normal stress components. In this regard, the nonlinear models (SA-RC-QCR2013 and RSM) performed better than the linear model (SA-RC), but none of the models was stellar. Predictions of $u'u'$ were particularly poor.

As part of the grid density study, CFD uncertainties due to discretization error were calculated. Near the junction separated region, very large CFD uncertainties underscored the lack of grid converged results and need for additional grid resolution for this separated flow. In future work, we will be testing both hand-refined grids as well as automated grid adaptation procedures for the Juncture Flow problem. We will also be expanding the computed solutions to include the wind tunnel walls.

Acknowledgments

The authors thank Robert Biedron of NASA Langley for his help with grid setup, and Henry Lee and Tom Pulliam of NASA Ames for computational support. Mike Wiese and Scott Brynildsen of the GEOLAB group at NASA Langley are acknowledged for their help with the CAD and gridding. The authors are also appreciative of all members of the Juncture Flow Team for their dedication throughout the course of the project. This work was supported by the NASA Transformational Tools and Technologies (TTT) project of the Transformative Aeronautics Concepts Program.

References

[1]Rumsey, C. L., Neuhart, D. H., and Kegerise, M. A., "The NASA Juncture Flow Experiment: Goals, Progress, and Preliminary Testing," AIAA Paper 2016–1557, January, 2016.

[2]Kuester, M. S., Borgoltz, A., and Devenport, W., "Experimental Visualization of Junction Separation Bubbles at Low- to Moderate-Reynolds Numbers," AIAA Paper 2016-3880, June 2016.

[3]Rumsey, C. L. and Morrison, J. H., "Goals and Status of the NASA Juncture Flow Experiment," NATO Science and Technology Organization, Specialists Meeting on Progress and Challenges in Validation Testing for Computational Fluid Dynamics, AVT-246-RSM-038, Avila, Spain, 26-28 September 2016, Paper Number AVT-246-03.

[4]Kegerise, M. A. and Neuhart, D. H., "Wind Tunnel Test of a Risk-Reduction Wing/Fuselage Model to Examine Juncture-Flow Phenomena," NASA/TM219348, November 2016.

[5]Lee, H. C., Pulliam, T. H., Neuhart, D. H., and Kegerise, M. A., "CFD Analysis in Advance of the NASA Juncture Flow Experiment," AIAA Paper 2017-4127, June 2017.

[6]Rumsey, C. L., Carlson, J.-R., Hannon, J. A., Jenkins, L. N., Bartram, S. M., Pulliam, T. H., Lee, H. C., "Boundary Condition Study for the Juncture Flow Experiment in the NASA Langley 14x22-Foot Subsonic Wind Tunnel," AIAA Paper 2017-4126, June 2017.

[7]Lee, H. C., Pulliam, T. H., Rumsey, C. L., Carlson, J.-R., "Simulations of the NASA Langley 14- by 22- Foot Subsonic Tunnel for the Juncture Flow Experiment," NATO Science and Technology Organization, AVT-284 Research Workshop on Advanced Wind Tunnel Boundary Simulation, Torino, Italy, 16-18 April 2018, Paper Number STO-MP-AVT-284-02.

[8]Rumsey, C. L., "The NASA Juncture Flow Test as a Model for Effective CFD/Experimental Collaboration," AIAA Paper 2018-3319, June 2018.

[9]Vassberg, J., Tinoco, E., Mani, M., Brodersen, O., Eisfeld, B., Wahls, R., Morrison, J., Zickuhr, T., Laflin, K., and Mavriplis, D., "Abridged Summary of the Third AIAA Computational Fluid Dynamics Drag Prediction Workshop," *AIAA Journal of Aircraft*, Vol. 45, No. 3, 2008, pp. 781–798.

[10]Anderson, W. and Bonhaus, D., "An Implicit Upwind Algorithm for Computing Turbulent Flows on Unstructured Grids," *Computers and Fluids*, Vol. 23, No. 1, 1994, pp. 1–22.

[11]Anderson, W., Rausch, R., and Bonhaus, D. L., "Implicit/Multigrid Algorithms for Incompressible Turbulent Flows on Unstructured Grids," *Journal of Computational Physics*, Vol. 128, 1996, pp. 391–408.

[12]NASA OVERFLOW CFD CODE, https://overflow.larc.nasa.gov, Accessed: 2018-10-31.

[13]Carlson, J.-R., "Automated Boundary Conditions for Wind Tunnel Simulations," NASA/TM-2018-219812, March 2018.

[14]Pirzadeh, S., "Progress Toward a User-Oriented Unstructured Viscous Grid Generator," AIAA Paper 96-0031, January 1996.

[15]Roe, P. L., "Characteristic-Based Schemes for the Euler Equations," *Annual Review of Fluid Mechanics*, Vol. 18, 1986, pp. 337–365.

[16]NASA FUN3D CFD CODE, https://fun3d.larc.nasa.gov, Accessed: 2018-10-31.

[17]Spalart, P. R. and Allmaras, S. R., "A One-Equation Turbulence Model for Aerodynamic Flows," *Recherche Aerospatiale*, Vol. 1, 1994, pp. 5–21.

[18]Shur, M. L., Strelets, M. K., Travin, A. K., Spalart, P. R., "Turbulence Modeling in Rotating and Curved Channels: Assessing the Spalart-Shur Correction," *AIAA Journal*, Vol. 38, No. 5, 2000, pp. 784–792.

[19]Mani, M., Babcock, D. A., Winkler, C. M., and Spalart, P. R., "Predictions of a Supersonic Turbulent Flow in a Square Duct," AIAA Paper 2013-0860, January 2013.

[20]Eisfeld, B., Rumsey, C., and Togiti, V., "Verification and Validation of a Second-Moment-Closure Model," *AIAA Journal*, Vol. 54, No. 5, 2016, pp. 1524–1541.

[21]Eisfeld, B., Rumsey, C., and Togiti, V., "Erratum: Verification and Validation of a Second-Moment-Closure Model," *AIAA Journal*, Vol. 54, No. 9, 2016, p. 2926.

[22]Spalart, P. R., "Strategies for Turbulence Modelling and Simulation," *International Journal of Heat and Fluid Flow*, Vol. 21, 2000, pp. 252–263.

[23]Celik, I. B., Ghia, U., Roache, P. J., Freitas, C. J., Coleman, H., Raad, P. E., "Procedure for Estimation and Reporting of Uncertainty Due to Discretization in CFD Applications," *Journal of Fluids Engineering*, Vol. 130, July 2008, 078001.

[24]Eça, L. and Hoekstra, M., "Evaluation of Numerical Error Estimation Based on Grid Refinement Studies with the Method of Manufactured Solutions," *Computers and Fluids*, Vol. 38, 2009, pp. 1580–1591.

[25]Yamamoto, K., Tanaka,K., Murayama, M., "Comparison Study of Drag Prediction for the 4th CFD Drag Prediction Workshop using Structured and Unstructured Mesh Methods," AIAA Paper 2010-4222, June 2010.

[26]Bordji, M., Gand, F., Deck, S., Brunet, V., "Investigation of a Nonlinear Reynolds-Averaged NavierStokes Closure for Corner Flows," *AIAA Journal*, Vol. 54, No. 2, 2016, pp. 386–398.

[27]Rumsey, C. L., "NASA Langley Research Center Turbulence Modeling Resource," https://turbmodels.larc.nasa.gov, Accessed: 2018-10-31.